Applied Geochemistry 196 (2026) 106650

Contents lists available at ScienceDirect

Applied Geochemistry

journal homepage: www.elsevier.com/locate/apgeochem

Reactive pathways of synthetic forsterite and Mg/Ni-serpentine: Insights into incipient dissolution and carbonation

Mattia Corti [a], Daniela D'Alessio [a], Mara Murri [b], Giancarlo Capitani [a], Marcello Campione [a,*], Nadia Malaspina [a,**]

[a] Department of Earth and Environmental Sciences, University of Milano-Bicocca, Milano, 20126, Italy
[b] Department of Earth and Environmental Sciences, University of Pavia, Pavia, 27100, Italy

ARTICLE INFO

Editorial handling by: Elisa Sacchi

Keywords:
Mineral carbonation
Microwave synthesis
Hydrothermal synthesis
CO_2 sequestration
Critical metal recovery

ABSTRACT

Carbon capture, utilisation and storage is among the key strategies to mitigate the increasing concentration of atmospheric carbon dioxide. Mineral carbonation stands out as a promising solution for long-term carbon sequestration by exploiting Ca–Mg-bearing oxides, hydroxides, and silicate minerals such as olivine and serpentine. Although the reaction occurs spontaneously in nature, it is strongly hindered by mineralogical and structural factors.

In this study, nanocrystalline pure forsterite and Mg- and Ni-endmember serpentines were synthesised as model phases to disentangle the role of composition, crystal structure, and morphology in incipient dissolution and carbonation and to maximise reactivity through increased surface-to-volume ratios. The choice of Ni-serpentine endmember aims to investigate the fate of Ni after dissolution and carbonation, considering that in nature serpentine can incorporate up to 0.5 wt% of nickel oxide. A systematic experimental strategy was designed to investigate their early-stage dissolution and carbonation behaviour under mild hydrothermal conditions (100 °C, $pCO_2 \leq 6$ bar), using microwave-assisted treatments in a controlled environment. The products were thoroughly characterised, both as solid precipitates and aqueous components, through X-ray Powder Diffraction, Scanning Electron Microscopy, Transmission Electron Microscopy, micro-Raman and Inductively Coupled Plasma – Optical Emission Spectroscopy. This direct, parallel comparison reveals distinct behaviours among the tested materials, with forsterite and Mg-serpentine releasing Mg into solution and promoting the formation of hydrated Mg-carbonates, whereas Ni-serpentine nanocrystals remain largely inert, immobilising Ni within their structure. These findings have potential implications not only for carbon dioxide sequestration but also for critical metal recovery processes.

1. Introduction

It is well known that the average concentration of carbon dioxide (CO_2) in the troposphere has experienced an increase of about 50 % due to anthropogenic activities during the last two centuries (IPCC, 2023). This has been recognised as a major factor responsible for a substantial enhancement of the greenhouse effect causing a steady positive drift of average temperatures around the globe (IPCC, 2023 and references therein). For this reason, in the last decades many studies focused on carbon capture, utilisation and storage (CCUS) as a possible solution to mitigate the large increase of CO_2 in the atmosphere. Our planet, in terms of geological reservoirs, can potentially sequester billions of tonnes of CO_2 per year acting as the largest laboratory available for long-term storage. Indeed, in geological reservoirs, CO_2 can be trapped by physical and chemical mechanisms. Among chemical mechanisms, mineral carbonation is emerging as a potential solution for virtually irreversible long-term carbon capture and storage. The idea consists of an accelerated form of water-mediated weathering of natural rocks, where the reaction of CaO- and MgO-bearing minerals (silicates, oxides and hydroxides) with water and CO_2 is spontaneous and exothermic (e.g., Berner et al., 1983; Lackner et al., 1995; O'Connor et al., 2002, 2004; Herzog, 2002; Hänchen et al., 2007; Matter and Kelemen, 2009; Lacinska et al., 2017). As an example, forsterite and serpentine reacting with CO_2 produce magnesite + quartz ± H_2O with $\Delta H = -88$ and -35

* Corresponding author.
** Corresponding author.
E-mail addresses: marcello.campione@unimib.it (M. Campione), nadia.malaspina@unimib.it (N. Malaspina).

https://doi.org/10.1016/j.apgeochem.2025.106650
Received 14 May 2025; Received in revised form 7 November 2025; Accepted 6 December 2025
Available online 8 December 2025

kJ/mol, respectively, and $\Delta Q = 24$ kJ/mol (at T = 515 K) and 78 kJ/mol (at T = 680 K) respectively (Lackner et al., 1995). These reactions proceed slowly in nature, particularly in ultramafic rocks (Kelemen and Matter, 2008), because several kinetic barriers pose great limitations to the reaction, unless catalytic geological processes occur locally, such as in serpentinites (Boschi et al., 2019). Indeed, reactivity depends dramatically on the crystal structure, surfaces exposed, along with the surface-to-volume ratio of the solid phase (Ide et al., 2007). For this reason, comparisons of reactivity among different minerals should refer to specific surfaces of minerals in single-crystal form. Up to date no experimental data on single crystals have been obtained to study the kinetics of serpentine carbonation, even if data on ex-situ carbonation reported by Sanna et al. (2014), comprising acidic treatments, indicate that the carbonation reaction efficiency of antigorite is 92 % compared to lizardite and olivine (66–81 %). This is likely due to the different reactive surface areas: 18.7 m^2/g for dehydrated antigorite, compared to 10.8 m^2/g for dehydrated lizardite and 4.6 m^2/g for olivine (O'Connor et al., 2001). Ex-situ mineral carbonation of serpentine therefore represents the future perspective for CO_2 mineralisation, particularly in nanocrystals or powdered minerals. However, traditional methods to accelerate carbonation, such as applying elevated temperature–pressure conditions (Kwak et al., 2011), thermal activation (McKelvy et al., 2004), or intensive grinding (Rashid et al., 2019), often achieve significant reaction rate increments but at the expense of high energy demand and operating costs. In contrast, as we will show in this work, the use of microwave-assisted treatments on nanocrystalline serpentines offers a more sustainable pathway, enhancing carbonation kinetics while maintaining energy efficiency.

Forsterite (Mg_2SiO_4, $2MgO \cdot SiO_2$) is an orthosilicate, with octahedrally coordinated Mg^{2+} and tetrahedrally coordinated Si^{4+}. O'Connor et al. (2002) carried out several carbonation experiments on natural samples of powdered olivine and serpentine, in aqueous solution, and at temperatures between 155 and 185 °C, and at CO_2 partial pressures up to 187 bar. At CO_2 partial pressure of 152 bar, olivine was observed to be more reactive than serpentine. Conversely, by heat treatment at temperature higher than 600 °C and high energy attrition grinding, the reaction between powdered serpentine and CO_2 was demonstrated to be more effective (Gerdemann et al., 2003). An enhanced carbonation of olivine and serpentine was achieved by some pioneering experiments employing a microwave (MW) hydrothermal equipment (White et al., 2004), and, recently, a systematic study of the reaction kinetics and the product obtained in the MW-driven carbonation of brucite allowed to identify key advantages in the use of radiative heating instead of thermal heating (Campione et al., 2024, 2025).

Serpentine [$Mg_3Si_2O_5(OH)_4$, $3MgO \cdot 2SiO_2 \cdot 2H_2O$] has a structure characterised by alternating layers of tetrahedral (T) silica (SiO_2) and octahedral (O) brucite-like [$Mg(OH)_2$] sheets (Yada and Iishi, 1974; Evans, 2004). Lizardite is the polytype having planar structure (Mellini, 1982), whereas chrysotile has tubular structure, in which TO-layers are wrapped up (Yada, 1971; Yada and Iishi, 1974, 1977; Wicks and Whittaker, 1975; Falini et al., 2004; Jancar and Suvorov, 2005; Lafay et al., 2013). Besides Mg and Fe, serpentine (along with olivine) is able to incorporate significant Ni concentrations in natural ultramafic rocks. In support to this ability, Baron et al. (2016) successfully synthesised the complete Mg–Ni-bearing serpentine solid solution, from lizardite [$Mg_3Si_2O_5(OH)_4$] to nepouite ($Ni_3Si_2O_5(OH)_4$) endmembers, with a MW-assisted hydrothermal apparatus. As far as we know, no study experimentally determined the rate of water-mediated carbonation of synthetic serpentine, and very few works have investigated the fundamental (micro- and nanoscale) understanding of the progression of this reaction, with a focus on the incipient stages (e.g., Sissmann et al., 2013). Rather, previous studies mainly focused on natural samples of olivine and serpentine, employing extreme experimental conditions and chemical treatments to permit complete conversion of the reactants, in accordance with the overall weak tendency of these minerals to react.

In this work, we deliberately use mild (hydrothermal) conditions to study the incipient dissolution and carbonation stages of synthetic well-defined models of forsterite and Mg- and Ni-serpentine. Considering that substitutions such as Ni^{2+}, Fe^{2+} and Fe^{3+} for Mg^{2+} and Al^{3+} for Si^{4+} can modify the structure of serpentine and its physical-chemical properties (Foresti et al., 2005; Bloise et al., 2009, 2010), hydrothermal synthesis of Mg- and Ni-serpentine end members, with progressively increasing heat treatment time, were carried out to understand the crystallisation pathways of serpentine and how the presence of Mg^{2+} or Ni^{2+} can modify the synthesis process and the final crystal morphologies. We synthesised forsterite by high-temperature calcination of a previously synthesised chrysotile/brucite mixture at hydrothermal conditions. To contrast the inertness of these phases, while ensuring the possibility to focus on the incipient stages of the reactions they are involved in, serpentine and forsterite were synthesised in the form of nanocrystals. This feature in fact promotes higher surface-to-volume ratios and substantially increases the mineral reactivity. Systematic hydrothermal treatments on the synthesised phases were carried out at 100 °C and at a partial pressure of N_2–CO_2 mixtures not exceeding 12 bar with the aid of a MW reactor, as described in Campione et al. (2024). The products of the performed treatments in the residual solid phase and in the dried supernatant liquid were analysed by X-ray Powder Diffraction (XRPD), Scanning Electron Microscopy (SEM), and Transmission Electron Microscopy (TEM). The amounts of Mg, Ni, and Si in the aqueous components were monitored as a function of the treatment duration and gas composition by Inductively Coupled Plasma-Emission Optical Spectroscopy (ICP-OES). This last step is of paramount importance as it can provide information on the fate of heavy metals such as Ni after the carbonation processes. Indeed, Ni and Cr can be mobilised after mineral carbonation reactions requiring mineral dissolution (Hamilton et al., 2018; Lu et al., 2022). The study of the behaviour of Ni-bearing serpentine during the first stages of carbonation could provide information on the possible applications of mineral carbonation and concurrent enhanced metal recovery as reported by Wang and Dreisinger (2022) for natural olivine.

Our results show that the structure and composition of the synthesised (versus natural) forsterite and of Mg- and Ni-serpentine have an important impact on the progress of carbonation, giving rise to specific inclinations to release in solution metal ions or the silica component. This kind of study has never been conducted, at least, on single minerals, and particularly at low temperature conditions, similar to those recorded in nature (hydrothermal conditions). Our results indicate that forsterite and Mg-serpentine exhibit similar reactivity toward CO_2. In contrast, Ni-serpentine appears to be a much more inert phase. In nature, Ni-serpentine can incorporate up to 0.5 wt% NiO in ultramafic bodies, more than 2 wt% in Ni-rich serpentine laterite soils, and up to 40 wt% in garnierite (Soler et al., 2008). In our experiments, Ni-serpentine produced fluids with metal concentrations about twenty times lower than those obtained from the Mg-endmember compounds. This opens new perspectives in the use of Mg-bearing silicates for CO_2 storage and in the exploitation of Ni-serpentine for Ni recovery.

Table 1
Quantities of reagents used for forsterite and Mg- and Ni-serpentine end member synthesis. In all syntheses deionised water is used as solvent.

Reagents	Forsterite	Mg-serpentine endmember	Ni-serpentine endmember
$Na_2SiO_3 \cdot 9H_2O$ (Sigma-Aldrich)	5.7 g	1.522 g	0.149 g
$MgCl_2$ (Sigma-Aldrich)	3.8 g	0.764 g	–
$NiCl_2 \cdot 6H_2O$ (Sigma-Aldrich)	–	–	0.187 g
NaOH solution (Carlo Erba Reagents)	350 ml, 0.4 mol l^{-1}	6 ml, 1.0 mol l^{-1}	2 ml, 1.0 mol l^{-1}

2. Materials and methods

Table 1 reports the mass of reagents, the volume and molarity of NaOH solutions used for all syntheses, which will be explained in the following sections. The concentration of NaOH determines the volume necessary to ensure the addition of a stoichiometric quantity (in the case of Mg- and Ni-serpentine synthesis) or an excess quantity (in the case of forsterite synthesis).

2.1. Forsterite synthesis

Following the experimental procedure proposed by Liu et al. (2018), the reagents (Table 1) were placed in a polypropylene liner and mixed. The liner was sealed, inserted into an autoclave reactor, and heated at 200 °C for 12 h in a furnace, to obtain a precursors mixture with the correct stoichiometry to produce forsterite. The liner contents were transferred to a set of centrifuge vials and centrifuged at 6000 rpm for 5 min. This procedure, followed by rinsing with deionised water, was repeated twice to remove the excess NaCl formed during the following reaction:

$$2MgCl_2 + Na_2SiO_3 + 2NaOH + 0.5H_2O \rightarrow 0.5Mg_3Si_2O_5(OH)_4 \text{ [serpentine]} + 0.5\ Mg(OH)_2 \text{ [brucite]} + 4NaCl \quad (1)$$

The precursor mixture was then dried at temperature of 110 °C for 4 h and ground to obtain a powder suitable for XRPD analysis. The forsterite precursor was subsequently transferred into a crucible and calcined at 900 °C for 4 h in a muffle furnace, to obtain the final product, *i.e.*, forsterite:

$$Mg_3Si_2O_5(OH)_4 \text{ [serpentine]} + Mg(OH)_2 \text{ [brucite]} \rightarrow 2Mg_2SiO_4 \text{ [forsterite]} + 3H_2O \quad (2)$$

The solid residue and dried supernatant collected after forsterite carbonation were also analysed with a SEM Gemini 500 (Zeiss), operating at 15 kV and 0.2 nA.

2.2. Hydrothermal synthesis of Mg- and Ni-serpentine endmembers

For Mg-serpentine synthesis, the starting material was a co-precipitated gel formed from the interaction between sodium metasilicate and an alkaline solution of Mg^{2+} (Monguzzi et al., 2014; Baron et al., 2016), in accordance with the following reaction:

$$2Na_2SiO_3 + 3MgCl_2 + 2NaOH \rightarrow Mg_3Si_2O_5(OH)_4 \text{ [chrysotile]} + 6NaCl + H_2O \quad (3)$$

The reagents were weighed according to the stoichiometry of reaction (3) and placed in a plastic vial with the addition of 9.0 ml of deionised water. Dispersion of the reagents was achieved by sonication of about 5 min, then centrifugation was performed at 6000 rpm for 5 min to separate the solid product (the co-precipitated gel) from the supernatant solution. Supernatant was removed, and the co-precipitated gel was rinsed with deionised water. The procedure was repeated to eliminate the excess NaCl. The co-precipitated gel, with addition of 220 ml of deionised water, was placed in a polypropylene liner with a volume of ~500 ml. The liner was closed, placed in the autoclave, sealed, and positioned in a furnace pre-heated at 45 °C with a setpoint temperature of 250 °C. Using this procedure, five different batches of co-precipitated gel were subjected to progressively increasing heat treatment times (2, 4, 6, 8, and 16 h).

For Ni-serpentine synthesis, the reagents (Table 1) were placed in autoclave, without any preparatory treatment. The synthesis reaction was as follows:

$$2Na_2SiO_3 + 3NiCl_2 + 2NaOH \rightarrow Ni_3Si_2O_5(OH)_4 \text{ [nepouite]} + 6\ NaCl + H_2O \quad (4)$$

Also in this case, five different batches were subjected to progressively increasing heat treatment times (2, 4, 6, 8, and 16 h) at a setpoint temperature of 250 °C.

After each synthesis, the liner contents were transferred to a set of centrifuge vials and centrifuged at 6000 rpm for 5 min, to separate the solid precipitate from the supernatant solution. Each solid product was analysed after exsiccation at 110 °C for 4 h. XRPD analysis of the solid products was carried out with a X'Pert Pro diffractometer (Malvern Panalytical), with a Bragg-Brentano geometry, using CuKα radiation (1.5417 Å) and operating conditions of 40 kV and 40 mA, and a divergence slit of 1/2°. The powder samples were back-loaded into flat sample holders, and XRPD patterns were collected over a 2θ angular range of 5–80°, with a step of 0.0167° and a counting time of 90 s/step.

The products obtained after 16 h of heat treatment of Mg- and Ni-serpentine syntheses were also analysed by TEM. Images were obtained with a JEOL JEM 2100 Plus TEM operating at 200 kV. A suspension of powdered materials dispersed in distilled water (3.0 μl) was dropped onto copper TEM grids with a 200-mesh framework (50 μm pitch) and diameter 3.05 mm, coated with a carbon support film.

2.3. Powdering of San Carlos olivine

Natural crystals classified as San Carlos Olivine (14.5 g) were ground using a Retsch vibratory mill in a 10 ml agate jar with six 7 mm agate grinding spheres, obtaining an ash-grey powder with a grain size of <20 μm. An XRD analysis was performed to characterise the sample.

2.4. Dissolution and carbonation experiments

Dissolution and carbonation of aqueous slurries of the powdered synthesised samples were performed using a MW synthesiser (SynthWave, Milestone) equipped with a mechanically stirred four-vial (glass, 40 ml capacity each) rack, housed in a Teflon-lined reactor with a total capacity of 900 ml filled with 200 ml of tap water (see inset in Table 2). Tap water was preferably used as the base load because it contains a fair concentration of electrolytes that facilitate the microwave absorption. The vials (total liquid volume is 30 ml) were filled with aqueous slurries of the nanominerals, prepared by adding a similar weight of the solid powders and an amount of water ensuring the same solid/water molar ratio (molality around 0.14 mol kg^{-1}, Table 2). This ensured good powder dispersion, considering that the weight should not exceed 0.5–1.0 g. Since forsterite, Mg-serpentine and Ni-serpentine have substantially different molecular masses (140.69, 277.11, 380.28 g mol^{-1}, respectively), the selected quantities represent the best trade-off between comparable powder mass and solid/liquid molar ratio.

The reactor was pressurised at room temperature (RT) by injecting 12 bar of N_2 (99.999 %) or a mixture of 6 bar of N_2 (99.999 %) + 6 bar CO_2 (99.995 %), as measured by a built-in pressure gauge. These pressures ensure a suitable excess of CO_2 when mixed with N_2 (see Campione et al., 2024 for details). In the former case, the use of pure N_2 allowed for hydrothermal treatments where only dissolution could occur. We therefore refer this set of treatments to as "dissolution experiments". In the latter case, the use of N_2/CO_2 mixtures enabled hydrothermal treatments where dissolution was enhanced, and simultaneous carbonate formation could occur. For simplicity, we refer to this set of treatments to as "carbonation experiments".

The mixture with N_2 and the relatively low partial pressures adopted were intended to use the CO_2 reactant in a dilute form and under conditions easily scalable to those available at industrial contexts (e.g., fuel gas, which can contain CO_2 with a concentration as high as 20 %). Reaction runs began with a linear heating ramp (heating stage) lasting 600 s until the setpoint temperature was reached, as measured by a temperature gauge immersed in the base load. Once the setpoint temperature was achieved, a dwelling stage of 1h followed (Table 2). After completion of the runs, the reactor was cooled by a water circuit running inside the reactor steel chamber to quench the reaction. Decompression was carried out at a temperature just below 65 °C, and the reactor

Table 2
Experimental set up for each 1h-run of hydrothermal treatments on synthesised Mg- and Ni-silicates under controlled partial pressure of N_2 and CO_2. The inset at the bottom shows a schematic image of the microwave synthesiser.

	Starting sample		Added deionised Water (ml)	Setpont Temperature (°C)	pCO_2 (bar)	pN_2 (bar)
Vial 1	Mg-serpentine	0.60 g	15	100	0–6	12–6
Vial 2	Ni-serpentine	0.54 g	10	100	0–6	12–6
Vial 3	forsterite	0.50 g	25	100	0–6	12–6
Vial 4	olivine (San Carlos)	0.50 g	25	100	0–6	12–6

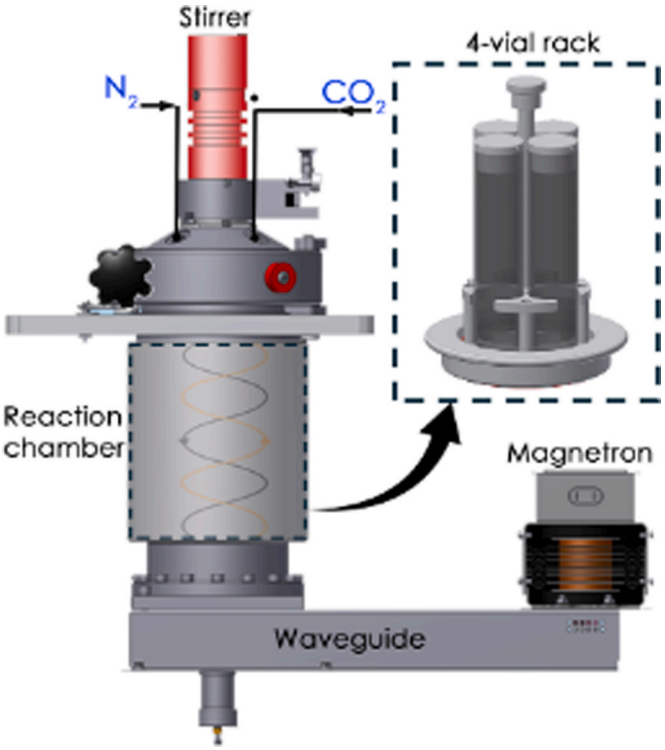

chamber was opened once it had cooled to below 35 °C. The vial contents after each run were transferred in a set of centrifuge vials and centrifuged at 6000 rpm for 5 min to separate the solid residue from the supernatant solution. The supernatant liquid was poured into another vessel. Each dissolution and carbonation experiment was repeated six times, using in each run (except the first) the solid residue obtained in the previous run and adding an appropriate amount of fresh deionised water according to Table 2.

Metal elements (Mg, Si, Ni) contained in supernatant solutions were determined by using an ICP OES Optima 7000 DV (PerkinElmer, Italy) system. Supernatant solutions were subsequently exsiccated at 50 °C in a thermostated furnace after pH measurement, to determine their dissolved electrolyte content. The dried residues were weighted and analysed by XRPD and Raman spectroscopy. Raman Spectroscopy analyses on the pristine and treated samples were carried out at the Experimental Mineralogy Laboratory "Fiorenzo Mazzi" (Department of Earth and Environmental Sciences, University of Pavia). Raman spectra were collected with a Horiba LabRam HR Evolution spectrometer (holographic gratings of 600 grooves mm^{-1}) equipped with an Olympus BX41 confocal microscope at a controlled temperature of 20(1) °C. Raman spectra were excited by the 532 nm line of a solid-state (YAG) laser. The laser power on the sample surface was approximately 10 mW. The spectrometer was calibrated to the silicon Raman peak at 520.5 cm^{-1}. The spectral resolution was ~2 cm^{-1} and the instrumental reproducibility in determining the peak positions was ~0.5 cm^{-1}. Data evaluation was performed using the OriginPro 2019 software package. The collected spectra were baseline-corrected for continuum luminescence background and normalised to acquisition time.

3. Results

3.1. Characterisation of the products of forsterite synthesis

The synthesis of chrysotile and brucite precursor mixture, and its subsequent calcination to obtain forsterite, proved successful, in agreement with Liu et al. (2018). In Fig. 1, the presence of NaCl (halite) is due to reaction (1). After calcination, a decrease in the precursor mixture mass was observed, due to water loss, as reported in reaction (4). Indeed, a 27.4 wt% water loss was measured (to be compared with 16.1 wt% expected based on reaction 4), which is slightly higher than the 22.5 wt% reported by Liu et al. (2018).

In addition to forsterite, as shown in Fig. 2, periclase and enstatite can occur in the calcined material, in accordance with the following reactions taking place during the calcination process:

$$Mg(OH)_2\ [brucite] \rightarrow MgO\ [periclase] + H_2O \quad (5)$$

$$Mg_3Si_2O_5(OH)_4\ [chrysotile] \rightarrow 2MgSiO_3\ [enstatite] + MgO + 2H_2O \quad (6)$$

$$MgSiO_3 + MgO \rightarrow Mg_2SiO_4\ [forsterite] \quad (7)$$

The XRPD pattern of the synthesised forsterite precursor (reaction 1) is characterised by the co-existence of two different phases (Fig. 1). One phase is represented by broader and less intense peaks, suggesting a partially disordered structure, at: 11.84° (d = 7.46 Å), 19.69° (d = 4.50 Å), 24.23° (d = 3.66 Å), 34.81° (d = 2.57 Å), 36.38° (d = 2.46 Å), and 60.25° (d = 1.53 Å), which correspond respectively to (002), (11-1), (004), (20-2), (202), and (061) of chrysotile (Falini et al., 2004). The other phase is represented by sharper and more intense peaks, at: 18.57° (d = 4.77 Å), 31.64° (d = 2.82 Å), 37.97° (d = 2.36 Å), 50.82° (d = 1.79

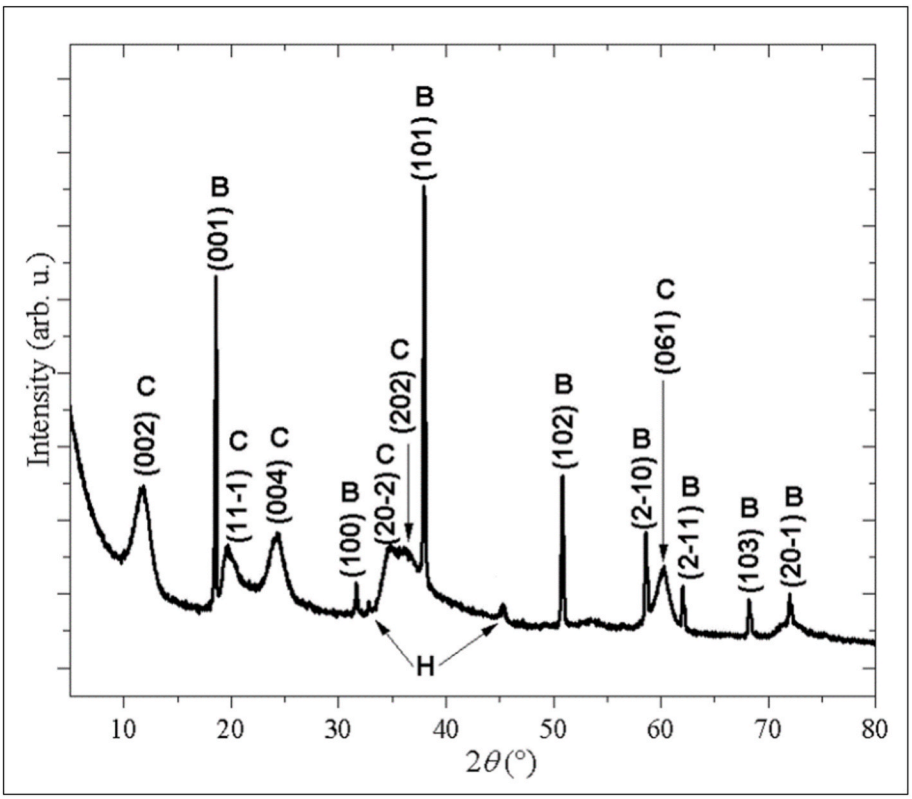

Fig. 1. XRPD pattern of forsterite precursor, after hydrothermal synthesis in autoclave, at 200 °C for 12 h. The product corresponds to a mixture of chrysotile (C) and brucite (B), with traces of halite (H). Peaks are identified and indexed using the reference structure by Falini et al. (2004), Catti et al. (1995) and Walker et al. (2004), respectively. Intensity in arbitrary units (arb. u.) of the ordinates axis is in linear scale.

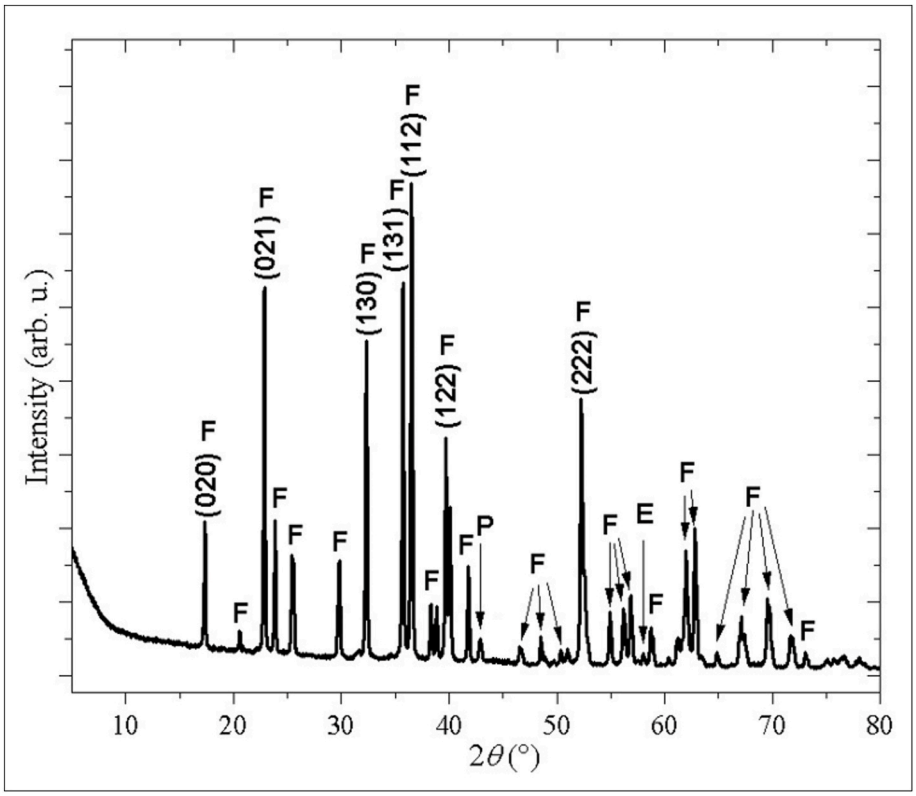

Fig. 2. XRPD pattern of the precursor phase (Fig. 1) after calcination at 900 °C for 4 h. Indexed peaks correspond to forsterite (F), with traces potentially attributable to periclase (P) and enstatite (E). Peaks are identified using the reference structures reported by Birle et al. (1968), Hazen (1976), and Hugh-Jones and Angel (1994), respectively. Intensity (arb. u.) of the ordinates axis is in linear scale.

Å), 58.59° (d = 1.57 Å), 62.03° (d = 1.49 Å), 68.19° (d = 1.37 Å), and 71.98° (d = 1.31 Å), which correspond respectively to (001), (100), (101), (102), (2–10), (2–11), (103), and (20-1) of brucite (Catti et al., 1995). Consequently, in accordance with reaction 1, synthesised forsterite precursor is a mixture of chrysotile, $Mg_3Si_2O_5(OH)_4$, and brucite, $Mg(OH)_2$. A minor phase is detected at 31.7°, and 45.4°, and identified as halite NaCl (Walker et al., 2004).

The total amount of synthesised forsterite precursor (3.97 g) was subjected to calcination at 900 °C for 4 h. According to the reaction (2), water was removed from the synthesised forsterite precursor, resulting in a substantial weight decrease (2.88 g), corresponding to 27.4 % water loss.

In the XRPD pattern of the synthesised forsterite precursor after calcination (Fig. 2), the most intense peaks at 17.33° (d = 5.11 Å), 22.85° (d = 3.88 Å), 32.26° (d = 2.77 Å), 35.67° (d = 2.51 Å), 36.46° (d = 2.46 Å), 39.63° (d = 2.27 Å), 52.18° (d = 1.75 Å), respectively corresponding to (020), (021), (130), (131), (112), (122) and (222), are attributable to forsterite (Birle et al., 1968).

Two secondary phases are detected at 42.92° and 58.04°, potentially ascribed to periclase, MgO (Hazen, 1976), and enstatite, $MgSiO_3$ (Hugh-Jones and Angel, 1994), respectively, although no other diagnostic peaks of both phases are observed.

To investigate the morphology of the synthesised forsterite, TEM images were acquired, showing clusters of subhedral particles with a maximum diameter of about 100 nm (Fig. 3).

To summarise, the adopted synthesis method allowed us to obtain forsterite mineral in the form of nanopowder. Trace amounts of periclase and enstatite were detected.

3.2. *Characterisation of the products of hydrothermal synthesis of Mg- and Ni-serpentine endmembers*

The XRPD patterns of the synthesised Mg- and Ni-serpentine end members (reactions 3 and 4) are shown in Figs. 4 and 5, respectively. Each spectrum represents an independent synthesis product, and not a time-monitored single batch. In Fig. 4, the bottommost curve shows the pattern of the co-precipitated gel (predominantly amorphous) with very broad reflections between 33 and 38°, and between 58 and 61°, potentially attributable to an incipient ordered stacking of the (202), (20-2) and (061) planes of Mg-serpentine (Falini et al., 2004). The product of 2 h-synthesis shows changes in the regions approximately between 18 and 30°, 35 and 40°, 58 and 65°, and 70 and 75°. In the first range, two peaks are visible at 19.82° (d = 4.47 Å), and 24.43° (d = 3.64 Å), whose positions match the interplanar distance of the (11-1) and (004) crystallographic planes of the reference structure. In the second range, the peak at 35.27° (d = 2.54 Å) may be ascribed to the (20-2) plane. In the third range, the reflection at 59.92° (d = 1.54 Å) is slightly downshifted with respect to the (330) plane. In the last range, a weak peak at 71.95° is visible, although its indexation is quite difficult. The XRPD pattern of the 4 h-synthesis product shows minor changes: peaks indexed as (11-1) and (004) are narrower, and the latter is downshifted to 24.34° (d = 3.65 Å). A low intensity peak at 38.04°, probably (101) of brucite (B, Catti et al., 1995), is observed.

In the 6 h-synthesis product, a peak at 11.93° (d = 7.41 Å), close to the (002) plane of the reference at 12.06°, appears. The ones at 18.67°, and 50.96°, are indexed as (001) (nominally at 18.58°), and (102) (nominally at 50.80°) of brucite, respectively. In the 8 h-synthesis product, the peaks are more intense and narrower, and brucite is no longer detected. The (002) peak is downshifted to 11.75°, and the peak at 60.27° (d = 1.53 Å) is consistent with (061) (nominally at 60.38° of reference). Another peak is observed at 36.20° (d = 2.47 Å), potentially corresponding to the (202) plane of the reference (nominally at 36.58°). In the 16 h-synthesis, (002) shifts to 12.00° (d = 7.36 Å), resulting in a better match with the reference structure. The (11-1) peak, previously at 19.82°, shifts to 19.65° (d = 4.51 Å), and (004) is at 24.26° (d = 3.66 Å); the peak at 36.20° shifts to 36.50° (d = 2.45 Å), corresponding to the (202) plane of the reference. Also in this case, peaks of brucite are detected.

The XRPD pattern of Ni-serpentine obtained after 2 h of hydrothermal treatment closely resembles that of Ni-serpentine end member nepouite (Brindley and Wan, 1975). It is characterised by high intensity, well-defined peaks at 11.88° (d = 7.43 Å), 19.67° (d = 4.51 Å), 24.54° (d = 3.62 Å), 34.02° (d = 2.63 Å), 36.00° (d = 2.49 Å), 60.50° (d = 1.53 Å), and 72.12° (d = 1.31 Å), which are potentially ascribed to (001), (110), (002), (200), (201), (060), and (261) of the reference nepouite structure (Fig. 2). In the 4 h-synthesis, (001) at 11.94° (d = 7.40 Å), (110) at 19.57° (d = 4.53 Å), (002) at 24.41° (d = 3.64 Å), (200) at 34.08° (d = 2.63 Å), and (060) at 60.54° (d = 1.53 Å) are more intense, narrower, and slightly shifted from the previous positions. In the 6 h-synthesis, no substantial changes are observed compared to the 4 h heat treatment. In the 8 h-synthesis, (001) at 12.08° (d = 7.31 Å), (110) at 19.64° (d = 4.51 Å), (200) at 33.97° (d = 2.63 Å), and (201) at 36.06° (d = 2.49 Å) are more intense and slightly shifted from the previous positions. A poorly defined peak at 42.23° (d = 2.14 Å), possibly corresponding to (132) of

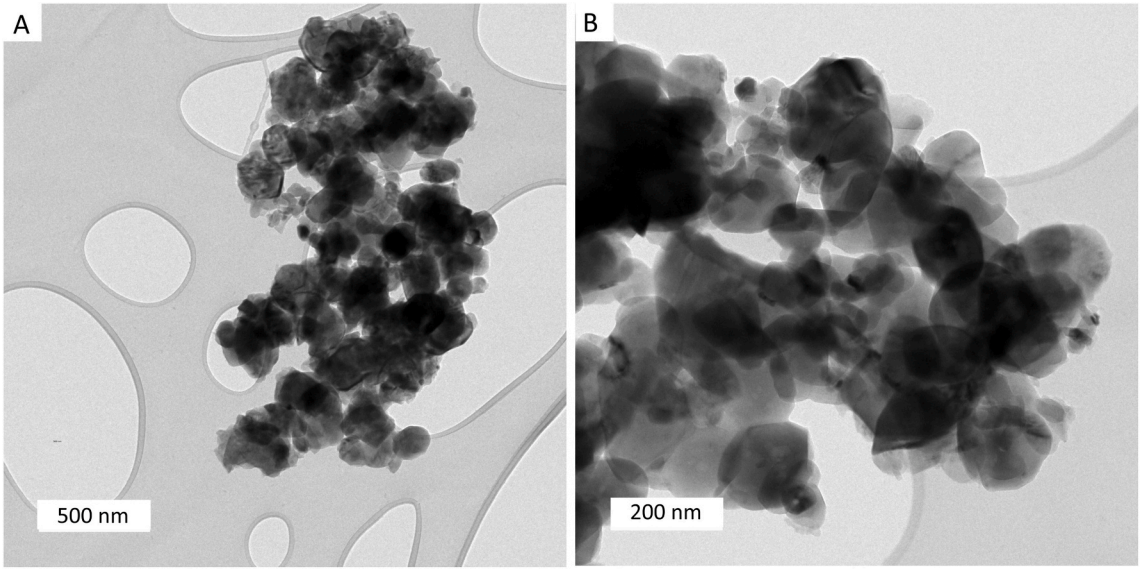

Fig. 3. Bright field TEM image of a cluster of particles representing the product of synthesis of forsterite.

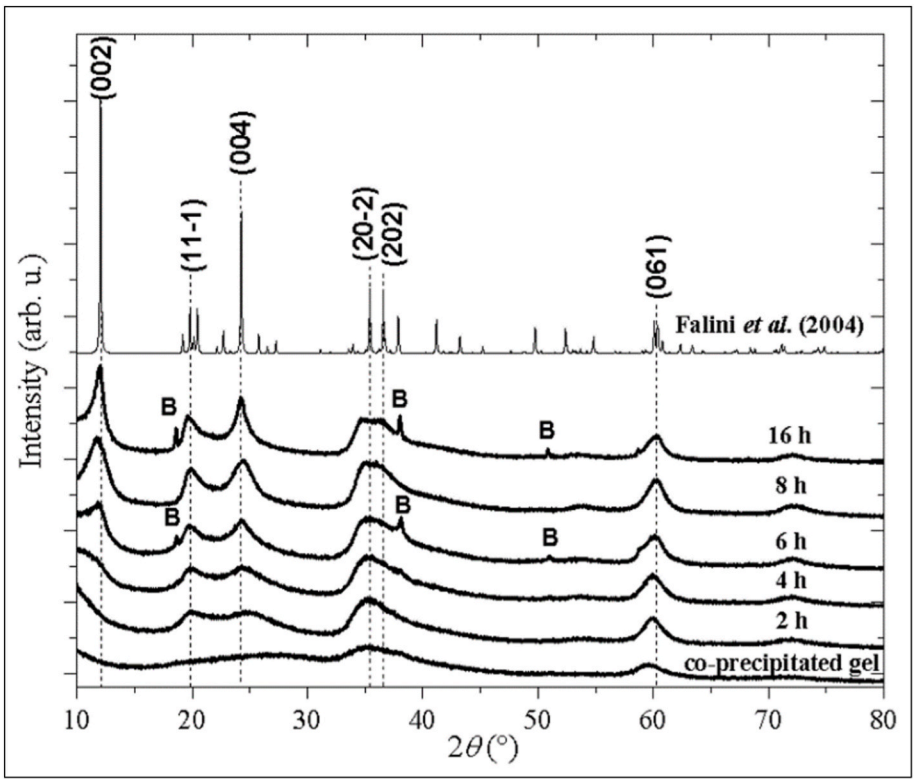

Fig. 4. XRPD patterns of the products of hydrothermal synthesis of Mg-serpentine end member, carried out at 250 °C with progressively longer heat treatment times, indicated on the right of each curve. The bottommost curve corresponds to the co-precipitated gel (without any heating process), obtained from the interaction between the reagents used for the synthesis series, and reported in Table 1. Products obtained after 2 and 4 h-synthesis show diffraction patterns resembling a "proto-serpentine" structure, as suggested by indexed peaks with reference structure of chrysotile (Falini et al., 2004). For heat treatments longer than 6 h, products correspond to Mg-serpentine end member. Peaks are identified and indexed using the reference of chrysotile (Falini et al., 2004), and B indicates the ones of brucite (Catti et al., 1995). Intensity (arb. u.) of the ordinates axis is in linear scale. Note that the broad peaks, even after long treatments, indicate that the mineral phases preserve their nanocrystalline morphology.

the reference, is observed. In the 16 h-synthesis, (001) shifts to 12.10° (d = 7.30 Å), (002) becomes more intense and shifts to 24.53° (d = 3.62 Å), and (132) becomes more defined.

To investigate the morphology of the synthesised serpentine phases, TEM images of Mg-serpentine and Ni-serpentine end members obtained after 16 h of synthesis at 250 °C were acquired. Fig. 6a and b shows nano*lamellae* of brucite and hollow cylindrical nanocrystals of Mg-serpentine endmember, respectively. Cylindrical nanocrystals have length of 20–300 nm and external diameter of 20–60 nm, showing the diagnostic nanotubular morphology typical of chrysotile. In Fig. 6c and d, nanocrystals correspond to Ni-serpentine end member, as shown by qualitative XRPD analyses (Fig. 5). Nano*lamellae* have diameters of 20–100 nm and are mostly hexagonal, whereas nanotubes are 60–100 nm long (with maximum lengths of 300–400 nm), slightly longer than chrysotile.

To summarise, our hydrothermal synthesis procedure for the Mg- and Ni-serpentine endmembers allowed us to obtain nanocrystalline phases of these minerals, predominantly showing a tube-like morphology for Mg-serpentine, and a mixture of lamellar and tube-like morphologies for Ni-serpentine. Minor amounts of brucite flake-like nanocrystals were occasionally found in the Mg-serpentine synthesis.

3.3. Dissolution and carbonation experiments

Table 3 reports the mass of solid residues collected after separation from the supernatant solution in each dissolution (12 bar N_2) and carbonation (6 bar N_2 + 6 bar CO_2) runs. These estimates are not meant to provide accurate indications on the dissolution progress, which rely on the results of ICP-OES, but rather to show that the molar ratio between the solid and the water varies within a range of 15–50 % at the beginning of each run.

The measured metal and silicon concentrations, as well as the metal/silicon molar ratios as a function of the number of 1h treatments, are reported in Fig. 7. Common features of the trends are the substantial increase of the solubilisation of all minerals in presence of CO_2 and the strong incongruency of solubilisation, both with and without CO_2. Moreover, concentrations tend to stabilise after the first run. Indeed, Mg-serpentine increases Mg concentration fourfold as a consequence of CO_2 injection, from about 5.0×10^{-3} to 2.0×10^{-2} mol l^{-1}. This increment is even more pronounced for Ni in Ni-serpentine (from 2.0×10^{-5} to 1.5×10^{-3} mol l^{-1}) and Mg in forsterite (from 8.0×10^{-4} to 3.0×10^{-2} mol l^{-1}). Similarly, Si increases its concentration with the presence of CO_2, although its concentrations are always lower than those of the other metals. On the other hand, while the solubilities of forsterite and Mg-serpentine are comparable, Ni-serpentine is almost 20 times less soluble (note the y-scales in Fig. 7A–D, G). Another distinctive feature of Ni-serpentine is that, in absence of CO_2, it is the only phase producing a supernatant solution composed almost exclusively of Si (reaching concentrations of 1.0×10^{-4} mol l^{-1}, Fig. 7H). In all other cases, the supernatant solution is enriched in the metal component, except for forsterite at later stages. In this respect, Mg-serpentine shows an exceptional behaviour, yielding relatively high levels of Mg in the supernatant even without CO_2, an extraordinarily high Mg/Si ratios (Fig. 7F).d with Si level as low as 5.0×10^{-6} mol l^{-1} (compared to 6.0×10^{-4} mol l^{-1} of forsterite), producing.

The Mg and Si concentration trends of olivine are similar to those of forsterite, although concentrations stabilise at values one order of

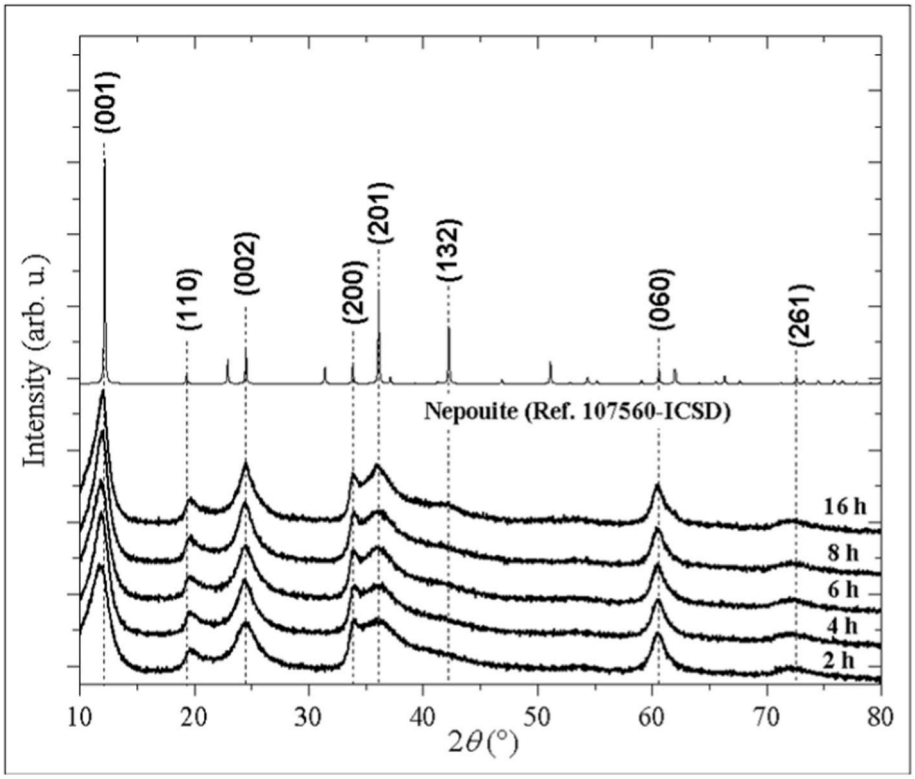

Fig. 5. XRPD patterns of the products of hydrothermal synthesis of Ni-serpentine end member, carried out at 250 °C with progressively longer heat treatment times, indicated on the right of each curve. Already after 2 h-synthesis, the product corresponds to Ni-serpentine end member and remains the same for longer heat treatments times (cf. sharp peaks with broad peaks of Fig. 4). Peaks are identified and indexed using the reference of nepouite structure (Brindley and Wan, 1975). Intensity (arb. u.) of the ordinates axis is in linear scale.

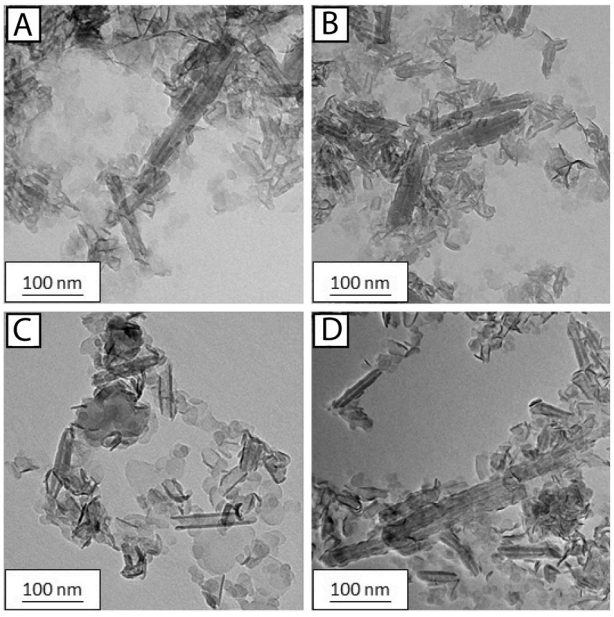

Fig. 6. Bright field TEM images of the products of hydrothermal synthesis of Mg- and Ni-serpentine end members, carried out at 250 °C for 16 h. A-B) Nano*lamellae* of brucite, and hollow nanotubes of chrysotile. C, D) Nano*lamellae* and hollow nanotubes of Ni-serpentine.

magnitude lower (Fig. 8). We attribute this effect to the larger average size and thus lower surface-to-volume ratios of the mineral particles, which also leads to a greater deviation of the Mg/Si ratio in the first run. The Ni concentration is as low as $\sim 10^{-7}$ mol l^{-1} after each run carried out without CO_2 and increases by two orders of magnitude in the presence of CO_2.

3.3.1. *Characterisation of solid residues after dissolution and carbonation experiments*

The comparison between the XRPD patterns of the untreated powders and of the solid residues obtained and dried after dissolution and carbonation experimental runs at 100 °C shows no detectable differences. The only exception is represented by Mg-serpentine, which, after the first run (both with and without CO_2) produces a pattern in which brucite peaks are absent, likely due to the higher solubility of this phase. This result corroborates the mild experimental conditions adopted, which involve only a transformation of the surface of the nanocrystallite surfaces without affecting their bulk crystallinity and structure, and without promoting the direct precipitation of detectable amounts of carbonate phases.

3.3.2. *Characterisation of the carbonate phases produced by exsiccation of supernatant solutions subjected to carbonation*

After each carbonation run and separation of the solid residue from the supernatant solution, the pH of the latter was measured with a pH meter (Hanna Instruments – Edge HI2002-02). As shown in Fig. 9, for forsterite and Mg-serpentine carbonated solutions, the pH ranges between 8.5 and 9.0, while for Ni-serpentine it progressively decreases, reaching 7.5. The pH trend measured for olivine closely follows that of synthetic forsterite, with an average value roughly 0.5 pH units lower. The alkalinity of the supernatants of forsterite and Mg-serpentine is consistent with solutions enriched in hydrogen carbonate and carbonate anions, formed as a consequence of enhanced dissolution reactions, which, *e.g.*, for forsterite can be written as:

Table 3
Quantities (in grams) of weighted solid residues collected after dissolution and carbonation reactions.

Exp. Run	Forsterite, Mg_2SiO_4		Mg-serpentine, $Mg_3Si_2O_5(OH)_4$		Ni-serpentine, $Ni_3Si_2O_5(OH)_4$		Olivine	
	[140.69 g mol^{-1}]		[277.11 g mol^{-1}]		[380.28 g mol^{-1}]		[145–153 g mol^{-1}]	
	12 bar N_2	6 bar CO_2 + 6 bar N_2	12 bar N_2	6 bar CO_2 + 6 bar N_2	12 bar N_2	6 bar CO_2 + 6 bar N_2	12 bar N_2	6 bar CO_2 + 6 bar N_2
Initial mass	0.5 [0.14 mol l^{-1}]	0.5 [0.14 mol l^{-1}]	0.6 [0.14 mol l^{-1}]	0.6 [0.14 mol l^{-1}]	0.54 [0.14 mol l^{-1}]	0.54 [0.14 mol l^{-1}]	0.5	0.5
After run #1	0.54	0.49	0.63	0.53	0.49	0.52	0.49	0.48
After run #2	0.5	0.4	0.57	0.51	0.44	0.48	0.44	0.46
After run #3	0.48	0.37	0.54	0.54	0.39	0.47	0.39	0.45
After run #4	0.45	0.28	0.5	0.45	0.34	0.44	0.34	0.38
After run #5	0.43	0.24	0.49	0.44	0.29	0.44	0.29	0.38
After run #6	0.42	0.18	0.46	0.41	0.29	0.35	0.29	0.33

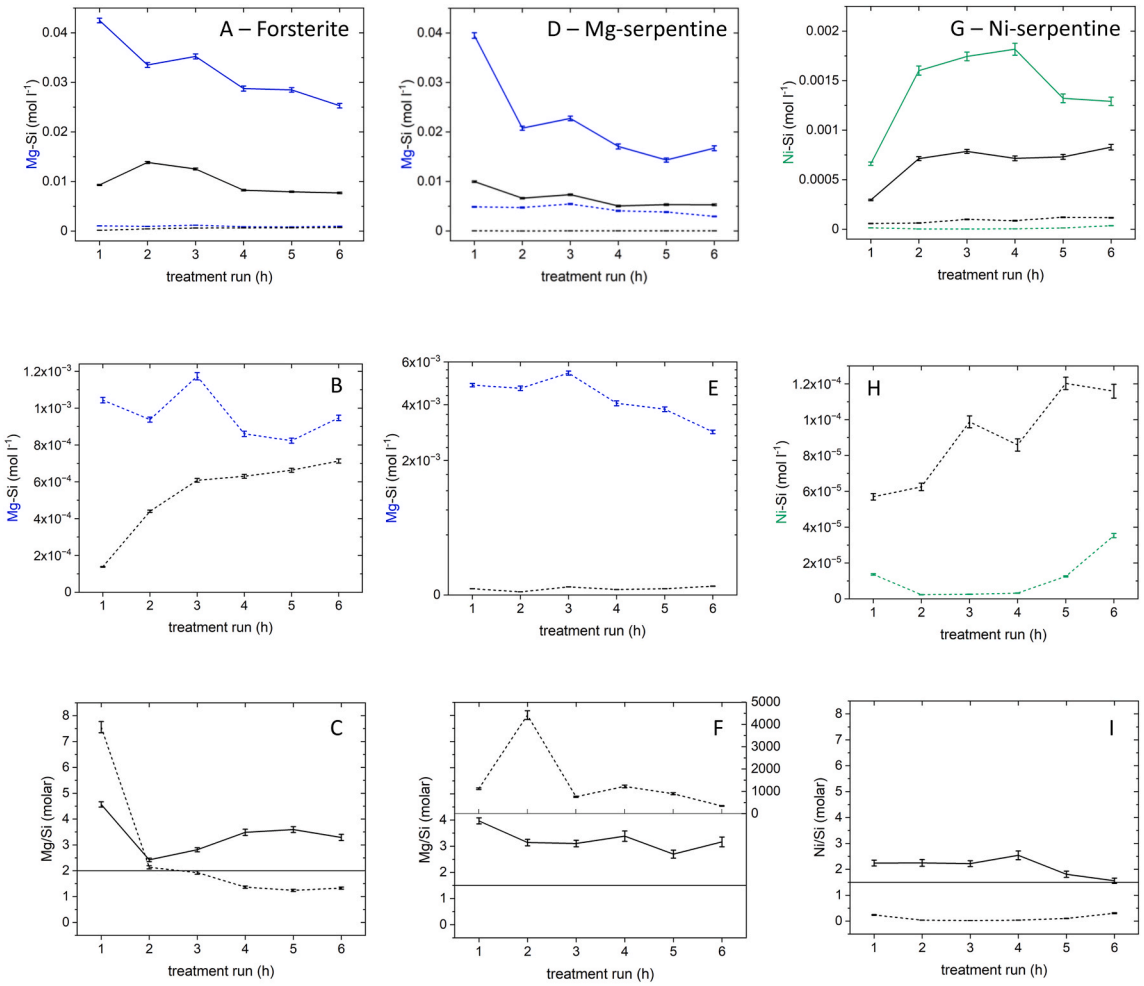

Fig. 7. Molar concentration of Mg (blue), Si (black), and Ni (green) as measured in supernatant solutions separated from forsterite (A and B), Mg-serpentine (D and E, the latter in square root scale), and Ni-serpentine (G and H) slurries prepared as illustrated in Table 2 and subjected to subsequent 1h-hydrothermal treatments at 100 °C with 12 bar N_2 (dashed lines) and a mixture of 6 bar N_2 + 6 bar CO_2 (solid lines). Related Metal/Si molar ratios are reported in panels C, F, and I, respectively. The solid horizontal lines indicate the molar ratio expected in the case of congruent dissolution (1.5 for serpentines and 2 for forsterite).

$$Mg_2SiO_{4,(s)}\ [\text{forsterite}] + 2CO_{2,(aq)} + \rightarrow 2\ Mg^{2+}_{(aq)} + 2CO^{2-}_{3,(aq)} + SiO_{2,(aq)} \quad (8)$$

$$Mg_2SiO_{4,(s)}\ [\text{forsterite}] + 4CO_{2,(aq)} + 2H_2O \rightarrow 2\ Mg^{2+}_{(aq)} + 4HCO^{-}_{3,(aq)} + SiO_{2,(aq)} \quad (9)$$

We attribute the lower pH value in Ni-serpentine supernatants to its lower solubility. Indeed, the cumulative masses obtained from the six exsiccated supernatants were 351 mg for forsterite, 24 mg for San Carlos olivine, 108 mg for Mg-serpentine, and only 6 mg for Ni-serpentine.

Exsiccation allows the attainment of saturation concentration of a family of mineral phases that, based on reactions (8) and (9), are expected to yield solid residues composed of carbonates and silica with various degrees of hydration (Norouzpour et al., 2025). Fig. 10 reports the XRPD and Raman spectra collected on the cumulative powders obtained after isothermal exsiccation at 50 °C of the six supernatants for each synthetic mineral.

The XRPD pattern collected on the forsterite sample (Fig. 10A) show the clear presence of a crystalline phase, together with a background signal indicating an amorphous phase. Given the good match with a reference structure provided by Raade (1970), the XRPD pattern reveals that the supernatant obtained from forsterite incipient carbonation

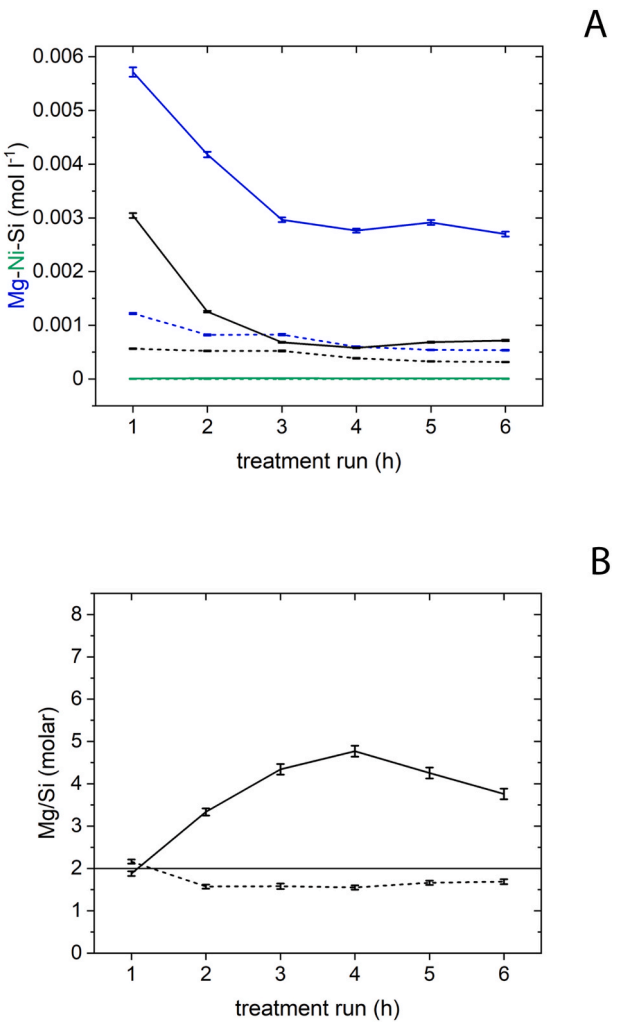

Fig. 8. (A) Molar concentration of Mg (blue), Si (black), and Ni (green) as measured in supernatant solutions separated from olivine slurries prepared as illustrated in Table 2 and subjected to subsequent 1 h-hydrothermal treatments at 100 °C with 12 bar N_2 (dashed lines) and a mixture of 6 bar N_2 + 6 bar CO_2 (solid lines). (B) Related Metal/Si molar ratios as reported in the text. The solid horizontal lines indicate the molar ratio expected in the case of congruent dissolution.

precipitates as the hydroxy-carbonate hydrate dypingite, $Mg_5(CO_3)_4(OH)_2{\cdot}5H_2O$. The Raman spectrum collected on the same sample (Fig. 10B) shows a clear peak at ca. 1100 cm^{-1}, confirming the presence of a carbonate phase. Both spectra in Fig. 10A and B shows no evidence of forsterite, demonstrating the efficacy of the supernatant separation procedure and suggesting the precipitation of the silicon component as amorphous silica.

The XRPD pattern collected on the Mg-serpentine sample (Fig. 10C) corresponds mainly to an amorphous phase. However, the very weak identifiable peaks are again consistent with dypingite. The presence of a carbonate phase is clearly demonstrated by the Raman spectrum (Fig. 10D), which is very similar to that of the exsiccated forsterite solution.

Finally, the XRPD pattern collected on the Ni-serpentine sample (Fig. 10E) is very similar to that of the pristine synthetic phase, showing a high background due to the amorphous component and a very few weak additional peaks. Raman spectroscopy of the same sample provides evidence of a heterogeneous material, showing regions of the pristine phase (consistent with XRPD) and additional regions of a carbonate phase (Fig. 10F). We note that the presence of Na^+ and Cl^- ions from the synthesis precursors (see section 3.1) might play a minor role in determining the nature of the precipitated phases.

Based on the XRPD analysis, the exsiccated phase obtained from supernatant solutions derived from olivine carbonation results in amorphous silica (Fig. 11A). However, Raman analysis allows the identification of a clear signal attributable to a carbonate phase (Fig. 11B).

4. Discussion

4.1. Structural properties of hydrothermal synthetic Mg- and Ni-serpentine endmembers

As shown by the XRPD pattern in Fig. 4, the co-precipitated gel is predominantly amorphous. However, the two broad reflections in the short-range order between 33 and 38°, and 58 and 61° suggest a partially ordered structure, even before the hydrothermal treatment for the synthesis of the Mg-serpentine endmember. Therefore, the presence of these diffraction peaks may indicate that T-sheets are already ordered at early stages.

After 2h of synthesis, we observed an evolution of the diffraction pattern, with two new peaks sub-perpendicular and parallel to the basal plane (Fig. 4). The (11-1) plane could be linked to the formation and ordering of the octahedral O-sheet, with $Mg(OH)_2$ composition, while the appearance of (004), potentially containing a TO-layer, could be related to the formation of the TO-structure itself (Fig. 4). The simultaneous formation of (11-1) and (004) may correspond to the development of the double-layered structure of the serpentine, whereas the absence of (002) (*i.e.*, the basal plane) suggests that single TO units are formed but not completely organised, since their stacking is not yet observed.

The product obtained after 4 h of synthesis shows no substantial differences with the previous one. Both materials cannot be defined as Mg-serpentine endmember because of the absence of (002), and can thus be classified as proto-serpentine (PS), considered a precursor of serpentine minerals and previously described as an amorphous or poorly crystalline material from which serpentine starts to grow (Yada and Iishi, 1974; Devouard et al., 1997; Grauby et al., 1998; Viti and Mellini, 1998; Normand et al., 2002; Andreani et al., 2004, 2007, 2008). Lafay et al. (2013) obtained PS with a flake-like morphology, together with brucite, after 2 h of synthesis in an autoclave at 300 °C and observed PS stability up to 3 h of reaction time and brucite disappearance after 8 h, when only chrysotile was detectable. Since (004) appears before (002), we agree that PS has a planar, flake-like morphology (Jancar and Suvorov, 2005; Lafay et al., 2013).

In the XRPD patterns of the products after 6, 8, and 16 h of synthesis, (002) is observed as a result of TO-layer stacking. This is diagnostic of Mg-serpentine endmember formation. The 2θ position of (002) tends to increase, although not systematically, from the 6 h product to final one. The shift of (002) towards values close to 12°, similar to the reference value (Falini et al., 2004), suggests a progressive decrease in d_{002}, which could correspond to a shrinkage of the TO layers structure of Mg-serpentine as synthesis time progresses. From the TEM images (Fig. 6), Mg-serpentine collected after 16 h of synthesis shows only nanotube morphology, and can thus be defined as chrysotile (specifically, nano-chrysotile).

Jancar and Suvorov (2005) obtained a serpentine-like structure before the effective appearance of chrysotile, with a flake-like morphology similar to the PS observed by Lafay et al. (2013, 2016). It was proposed that chrysotile crystallisation starts from the early flake-like nanocrystallites of PS. The latter shows a double layer TO-structure and continues growing with time until a threshold size is reached, at which point a "curling"-like process starts, leading to nanotube formation (Jancar and Suvorov, 2005). Moreover, chrysotile was reported to crystallise from dissolution of PS and brucite, through a dissolution-reprecipitation mechanism consistent with Ostwald ripening. Considering these chrysotile crystallisation pathways, our

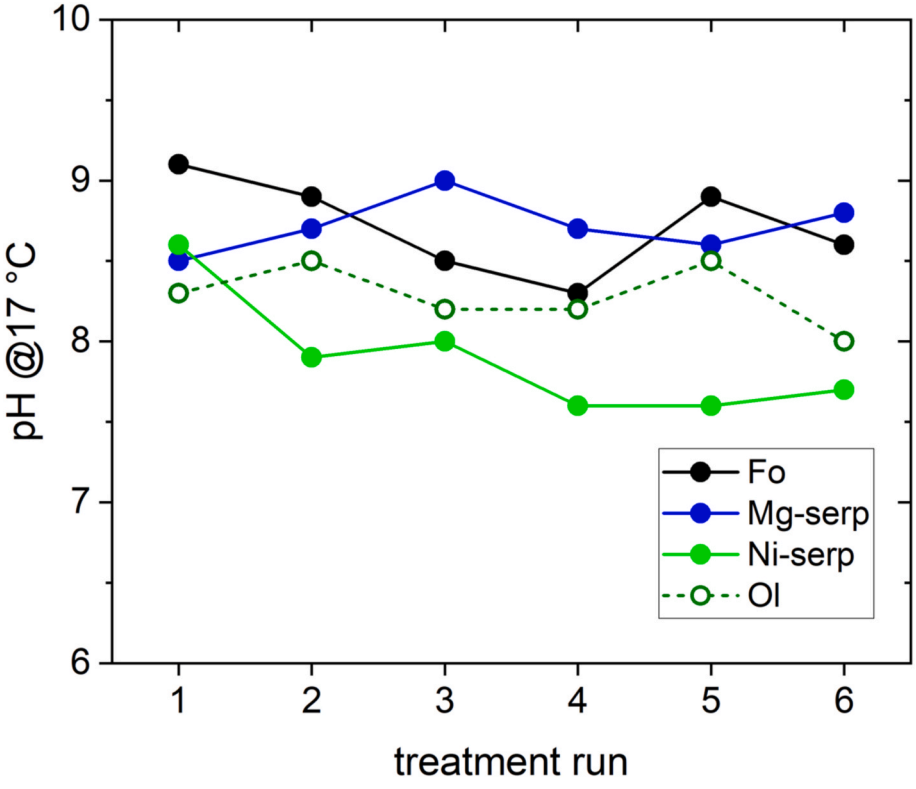

Fig. 9. pH measured at 17 °C of the supernatant solutions after the carbonation treatments of the synthesised minerals: forsterite (black), Mg-serpentine (blue), Ni-serpentine (light green), and San Carlos olivine (dark green, dashed line).

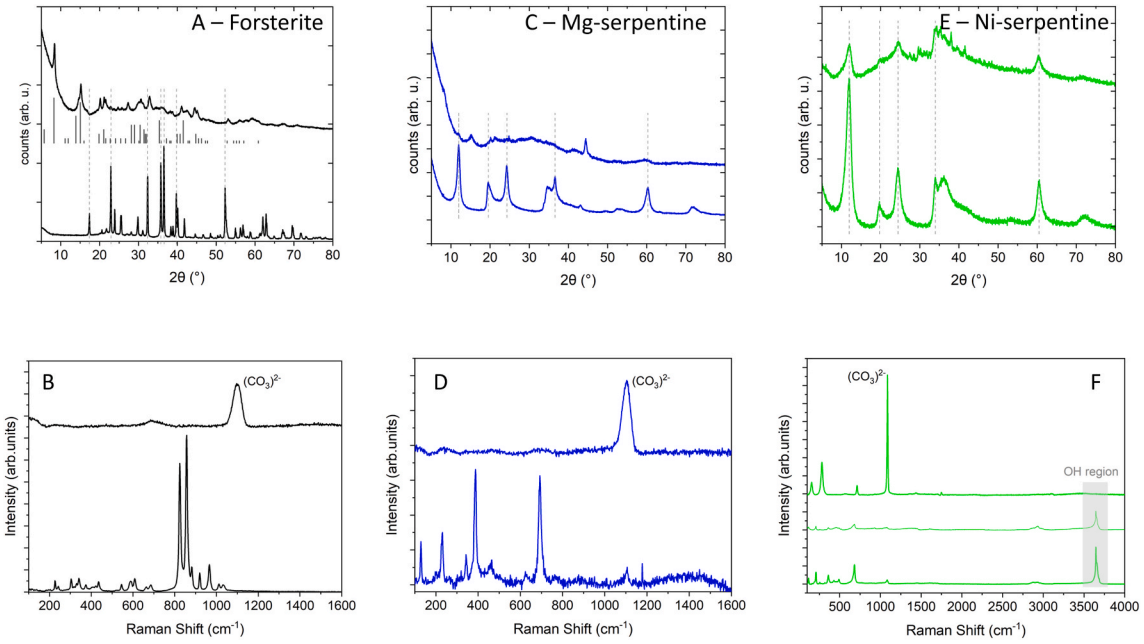

Fig. 10. XRPD (A, C, E) and Raman spectra (B, D, F) collected on pristine synthetic samples (lower line in each panel) and exsiccated supernatant solutions (upper line) obtained after the carbonation treatments. The histogram in A reports the intensity lines known for the dypingite structure reported by Raade (1970). In panel F, two representative spectra of the exsiccated supernatant collected in different areas of the powder are displayed.

XRPD and TEM analyses suggest that the stacking of TO-layers is concomitant with the curling of the initial planar, flake-like PS, which displays only nanotubes morphology after 16 h of synthesis.

As shown in Fig. 5, the synthesis of Ni-serpentine endmember proceeds more rapidly than that of Mg-serpentine (*i.e.*, chrysotile). Already after 2 h of synthesis, the product exhibits an XRPD pattern compatible with Ni-serpentine endmember, *i.e.*, nepouite (Brindley and Wan, 1975).

The (001) plane of Ni-serpentine represents the basal plane, while the (200) plane is perpendicular to (001), and other planes are sub-perpendicular to the basal one. As already observed for the co-precipitated gel in Mg-serpentine synthesis, the planes perpendicular or sub-perpendicular to the basal one could be related to the formation

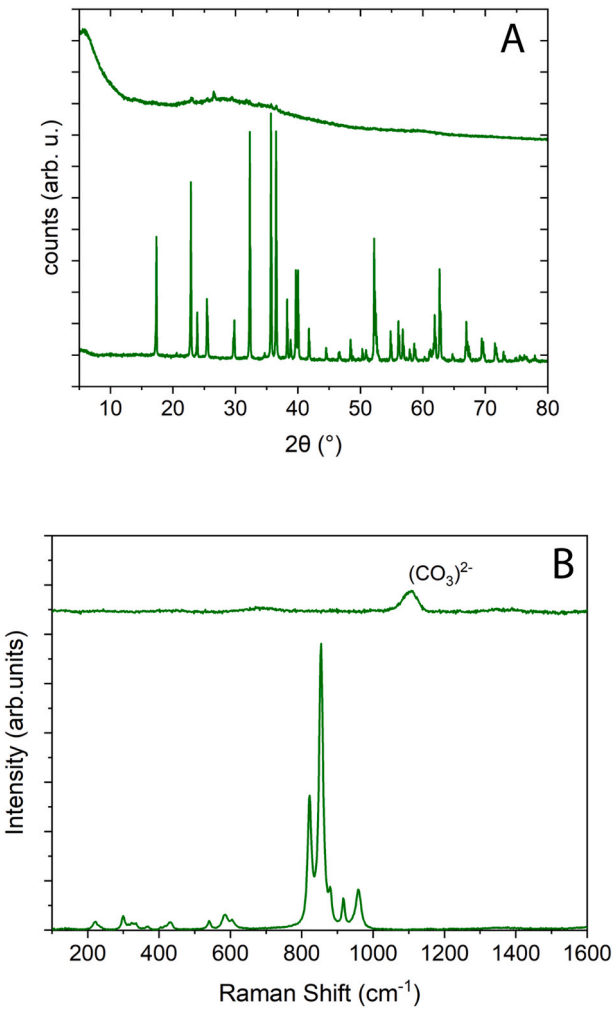

Fig. 11. XRPD (A) and Raman spectra (B) collected on pristine San Carlos Olivine (lower line in each panel) and exsiccated supernatant solutions (upper line) obtained after its carbonation treatments.

of Si–O–Si bonds, and then to the individual SiO_4 tetrahedra forming the T-sheet. Similarly to the (004) plane in chrysotile, the (002) plane is suggested to be associated with the formation of single TO-unit, where the O-sheets have $Ni(OH)_2$ composition. The (001) and (002) planes are observed concurrently.

Subsequent syntheses (4, 6, 8, and 16 h) show a progressive shift of the peaks, likely explained by the shrinkage of the TO structure of Ni-serpentine as synthesis time progresses. TEM analysis (Fig. 6C and D) shows that Ni-serpentine after 16 h of synthesis displays a more complex morphology (nano*lamellae*, and nanotubes), whereas for Mg-serpentine after 16 h of synthesis exhibits only nanotubes.

Previous studies on Ni-doped systems aimed to synthesising Ni-serpentine phases (Korytkova et al., 2005a, 2005b; Korytkova and Pivovarova, 2010; McDonald et al., 2009; Bloise et al., 2010) demonstrated that several parameters (temperature, time, pH, pressure, and Ni content) play important roles in determining morphology and size during Ni-serpentine synthesis (Bloise et al., 2010). Korytkova et al. (2005a) obtained $(Mg,Ni)_3Si_2O_5(OH)_4$ nanotubes from NiO and MgO, and $Ni_3Si_2O_5(OH)_4$ nanotubes from $NiSiO_3$ and MgO, both at 400 °C and 70 MPa. McDonald et al. (2009) synthesised Ni-serpentine endmember nanotubes from a mixture of Ni-chloride, silicic acid, and NaOH, in autoclave for 18 h at 250 °C and 10 MPa.

The comparison between Mg-serpentine and Ni-serpentine endmember syntheses shows that the complete substitution of Mg^{2+} by Ni^{2+} can promote and accelerates both nucleation and crystallisation. In this study, chrysotile formation is preceded by the precipitation of a metastable phase (PS), stable up to 4 h. After 6 h, stacking of the previously formed single TO layers begins, leading to curling and the development of nanotubular morphology from the earlier flake-like PS structure. Conversely, as noted above, the Ni-serpentine endmember is already obtained after 2 h of synthesis, without passing through the metastable PS stage, as observed for chrysotile. Moreover, Ni maintains the serpentine structure planar for a longer time (possibly until 6 h) and indeed d_{001} remains between 7.40 and 7.43 Å. For prolonged reaction time (8, and 16 h) the curling process occurs, and d_{001} decreases to 7.30 Å. However, this transformation occurs more slowly than in the Mg-serpentine 16 h synthesis. In the former case, nano*lamellae* are still visible, whereas in the latter only nanotubes appear.

The different kinetics and morphology between Mg-serpentine and Ni-serpentine endmembers can be explained by the different bonding length of Mg–O and Ni–O within the octahedral O-sheets, and the consequent lateral mismatch with the tetrahedral T layer. For the Mg-serpentine endmember (*i.e.*, chrysotile), the mismatch is greater and compensated by the curling of TO layers after 6 h of synthesis, whereas for Ni-serpentine the mismatch between O and T-sheets is smaller, and the curling process takes place only at later times. These observations agree with Korytkova and Pivovarova (2010), who proposed that the cation in the octahedral O-sheets of the serpentine structure is the main factor determining the mechanism and rate of nanotubes formation, as well as of their morphology and sizes. The kinetics of Mg- and Ni-serpentine nucleation and crystallisation, and the shape of the resulting nanocrystals, have important implications in the incipient dissolution and carbonation reaction discussed below.

4.2. Dissolution and carbonation experiments

In chrysotile nanotubes, the outermost sheet is in principle purely octahedral, having a $Mg(OH)_2$ composition, whereas the inner surface has a purely silica composition. This characteristic may explain the surprisingly high tendency of this mineral phase to release Mg even in neutral environments (Fig. 7D, E, F; Lesci et al., 2014). This structural motif also holds in the case of Ni-serpentine nanotubes. However, as observed in Fig. 7G and H, Ni is far less prone to be released from the octahedral layer. Under neutral conditions, the tetrahedral layer appears weaker than that of chrysotile (as indicated by the higher concentration of Si in solution), whereas under acidic conditions both tetrahedral and octahedral layers appear stronger. This behaviour can be in general explained by the lower reactivity of the $Ni(OH)_2$ component with respect to $Mg(OH)_2$ and by the morphological and structural features discussed in section 4.1 and illustrated in Fig. 6. Indeed, the leaching of $Ni(OH)_2$ is much more difficult due to the stronger Ni–OH bonds and the tighter TO-layer structure (d_{001} = 7.30 against 7.43 Å of chrysotile). Since the O- and T-sheets are interlayered, the O-layers in nepouite exert a protective effect on the T-sheets, making them less leachable than those in chrysotile. On the other hand, the more planar morphology of our Ni-serpentine sample (Fig. 6) makes the T-layer more exposed to the external environment, explaining the higher Si concentration under neutral environment.

The action of CO_2 on the O-layers is illustrated by the following reaction:

$$M(OH)_{2,s} + CO_{2,aq} \rightarrow M^{2+}_{aq} + CO^{2-}_{3aq} + H_2O;\ M = Mg^{2+},Ni^{2+} \quad (10)$$

Subsequently, once the O-layer is removed from the nanotubes or nanolamellae, the exposed surface is composed of the polymerised T-sheet of $[Si_2O_5]^{2-}$ units, which are less reactive to CO_2, causing a decrease or stabilisation of the dissolution rate.

Forsterite, being an orthosilicate, is expected to exhibit substantial differences in its dissolution dynamics compared to phyllosilicates. In neutral environment, forsterite releases a constant amount of Mg, much lower than chrysotile, and a slowly increasing amount of Si (much

higher than chrysotile, Fig. 7B). Forsterite is the only sample displaying a Mg/Si trend crossing the congruency, from Mg-excess at early times, to Si-excess at late times (Fig. 7C). This means that the solid residue, similarly to serpentines, tends to be Si-enriched, but unlike serpentines, this silica component is more soluble than that formed by serpentines. This is reasonable, since silicate groups are not polymerised in forsterite and do not tend to polymerise under neutral conditions (Pokrovsky and Schott, 2000). Their solubilisation is therefore facilitated.

Surprisingly, under CO_2-rich conditions, the behaviour of forsterite closely resembles that of chrysotile. Indeed, concentration trends of Mg and Si are almost superimposable (Fig. 7A–D). In such environment, the process of dissolution of forsterite starts with an exchange of two H^+ in the acidic solution with one Mg^{2+} on the forsterite surface, followed by the formation of $[Si_2O_7]^{6-}$ dimers, which, in turn, can adsorb an additional proton, promoting dissolution of the silica layer. Hence, this mechanism leads to the formation of a superficial silica-rich layer depleted in Mg^{2+}, which is then released into the solution (Pokrovsky and Schott, 2000; Daval et al., 2011). The polymerisation induced by the acid catalyser produces apparently a solid residue with similar chemical properties as that produced by leaching of chrysotile. Several authors pointed out that a passivation process may take place around serpentine grains within the aqueous reaction environment, after sample leaching. This prevents the sample from further chemical etching but also hinders the metal ion release and the occurrence of carbonation reaction, i.e. the above-mentioned cations to precipitate as carbonate phases (Jonckbloedt, 1998; Park et al., 2003; Alexander et al., 2007). This behaviour might be reflected even at early stages of carbonation by the observed decreasing trend of the concentration of Mg ions (Fig. 7A–D), which, however, seems not to be the case for Ni-serpentine (Fig. 7G).

4.3. Carbonate phases precipitated from dried supernatant solutions

In the case of synthesised forsterite and Mg-serpentine, the carbonate phase precipitated from the solutions after the carbonation treatment was identified as dypingite. In this respect, we underline that dypingite should be regarded as a series of phases with varying degrees of hydration rather than a single, well-defined phase. Its specific characteristics, such as diffraction peak positions, depend on the hydration degree, which in turn is related to the evolution of the carbonation reaction (Yamamoto et al., 2022). Further support for this interpretation is provided by theoretical kinetic models of early-stage olivine dissolution in the presence of CO_2 (Shikazono et al., 2014), which identified the formation of artinite, $Mg_2(CO_3)(OH)_2{\cdot}3H_2O$ (Akao and Iwai, 1977), a hydroxy-carbonate with a different degree of hydration. Consistent with the primary role played by the octahedral sheet in chrysotile, both dypingite and hydromagnesite are observed as direct products of pure brucite carbonation at 100 °C. The corresponding dried supernatant solutions give rise to mixed hydromagnesite–dypingite phases, with proportions depending on the drying temperature (Campione et al., 2024).

To tentatively assign the unidentified carbonate phase(s) in the case of synthesised Ni-serpentine endmember, we rely solely on the chemical composition of the studied system. Indeed, the literature reports XRPD patterns of natural samples of hydrated Ni-carbonates, which do not completely match our experimental XRPD data. A possible explanation is that our experiments involved synthesised nanocrystals, likely exhibiting different lattice and crystal morphologies, which could have led to a distinct reaction pathway. Consequently, we speculate that hydrated Ni-carbonates are among the products formed in the dried supernatant fraction of the synthesised Ni-serpentine endmember carbonation at 100 °C (reported in Fig. 10E and F).

The side-by-side evaluation of forsterite, Mg-serpentine, and Ni-serpentine endmembers provides a novel framework for disentangling the respective roles of crystal structure and composition in controlling early-stage dissolution and carbonation. While forsterite and Mg-serpentine share a propensity to release Mg and favour carbonate precipitation, Ni-serpentine exhibits sluggish reactivity and strong Ni retention, highlighting the contrasting behaviours of structurally related silicates. Such parallel testing under the same experimental conditions provides a unique benchmark for interpreting mineral reactivity and guiding the selective use of ultramafic materials in CCUS and metal-recovery strategies.

4.4. Implications for the use of ultramafic phases in CCUS processes

The systematic comparison of forsterite, Mg-serpentine, and Ni-serpentine highlights how subtle differences in crystal structure and composition translate into markedly different behaviours during early-stage carbonation. Forsterite and Mg-serpentine exhibit a clear propensity to dissolve and release Mg, which in turn promotes the precipitation of hydrated Mg-carbonates. This confirms their potential as efficient feedstocks for CO_2 sequestration, particularly when present as fine-grained or nanocrystalline phases that maximise reactive surface area.

By contrast, Ni-serpentine shows sluggish dissolution, retains Ni within its lattice, and produces solutions with metal concentrations nearly an order of magnitude lower than those generated by Mg-serpentine or forsterite. This inertness implies limited effectiveness of Ni-serpentine in accelerating carbonation, but at the same time points to its ability to immobilise Ni and thus restrict its mobility during mineral–fluid interactions. This dual behaviour has direct implications for both CCUS and environmental management: Mg-rich serpentinites can be prioritised for rapid carbonation and CO_2 uptake, while Ni-bearing serpentinites may instead play a role in long-term metal immobilisation, limiting the release of potentially critical or toxic elements.

From an applied perspective, the exploitation of serpentinite quarry waste, particularly from industrial districts such as Valmalenco, Italian Central Alps (Cavallo, 2018), represents a unique opportunity to couple CCUS deployment with circular economy goals. The large amounts of Mg-rich waste generated annually (e.g., serpentine, relict olivine and orthopyroxene, chlorite) could be transformed from an environmental burden into a strategic resource for CO_2 mitigation, while simultaneously producing carbonate and silica by-products for various industrial markets.

Our findings underscore the need to discriminate among ultramafic phases when evaluating natural or industrial feedstocks for carbonation. Materials dominated by Mg-serpentine and forsterite are expected to contribute most effectively to CO_2 capture, whereas the presence of significant Ni-serpentine fractions may lower carbonation efficiency but simultaneously stabilise Ni within the solid phase. Such knowledge is essential for the rational design of CCUS strategies that balance the objectives of carbon sequestration, resource recovery, and environmental safety.

5. Conclusions

This study investigated the dissolution and carbonation behaviour of synthetic nanocrystals of forsterite and Mg- and Ni-serpentine endmembers. The adopted synthesis routes yielded well-defined nanocrystals, allowing us to disentangle the role of crystal structure, morphology, and composition under mild hydrothermal conditions.

Key findings are as follows:

1) Mg-serpentine nanotubes fully crystallise at 250 °C after 16 h, evolving from a metastable proto-serpentine phase, whereas Ni-serpentine nanocrystals reach complete crystallinity after only 2 h, without passing through this intermediate stage.
2) Forsterite and Mg-serpentine readily dissolve in CO_2-saturated water, producing undersaturated solutions that precipitate hydrated Mg-carbonates (mainly dypingite) upon exsiccation. Higher CO_2 pressures or longer reaction times are required to achieve full saturation.

3) The nanotubular structure exerts a major control on reactivity: the $Mg(OH)_2$-rich outer O-sheets of chrysotile-like Mg-serpentine dissolve easily even in neutral conditions, whereas the $Ni(OH)_2$ sheets in Ni-serpentine are significantly more resistant.
4) Carbonation of Ni-serpentine is sluggish or absent, resulting in strong Ni retention within the solid phase. Hence, mineral structure and cation chemistry critically govern carbonation kinetics and the fluid–solid partitioning of transition metals.

Beyond these specific results, this work provides the first direct, side-by-side comparison of forsterite, Mg-serpentine, and Ni-serpentine nanocrystals synthesised and tested under identical conditions. The systematic framework highlights how subtle structural and compositional differences dictate dissolution pathways, carbonation efficiency, and element mobility. Such insights establish a robust basis for assessing the selective reactivity of ultramafic phases in CO_2 sequestration and critical-metal recovery strategies.

CRediT authorship contribution statement

Mattia Corti: Writing – original draft, Methodology, Investigation, Formal analysis, Conceptualization. **Daniela D'Alessio:** Writing – review & editing, Methodology, Investigation, Formal analysis. **Mara Murri:** Methodology, Investigation. **Giancarlo Capitani:** Methodology, Data curation. **Marcello Campione:** Writing – review & editing, Supervision, Methodology, Investigation, Formal analysis. **Nadia Malaspina:** Writing – review & editing, Resources, Project administration, Funding acquisition.

Declaration of competing interest

The authors declare that they have no known competing financial interests or personal relationships that could have appeared to influence the work reported in this paper.

Acknowledgements

We thank Matteo Zippoli who helped in olivine calcination and carbonation experiments, Lucia Galimberti for her help in performing the calcination process and Fabrizio Vergani for assistance during SEM analyses.

We acknowledge funding by Cariplo Foundation "ANTI-CARB–Quarry waste ANTIgorite CARBonation: a zero emission platform for re-manufacturing with the benefit of CO2 sequestration" (Grant n. 2020-0977); N. Malaspina and M. Corti thank the Italian Ministry of University and Research project "Competing geological and biological processes in underground carbon and hydrogen storage" (Grant n. 20224YR3AZ). This work also benefited from the University of Milano-Bicocca "Redox processes and implications on C–O–H–S budget from the shallow crust to the deep mantle" (Grant n. 2022-ATEQC-0015). Part of the work was performed with the support of Project MIUR - Dipartimenti di Eccellenza TECLA, Department of Earth and Environmental Sciences, University of Milano-Bicocca.

Data availability

Data will be made available on request.

References

Akao, M., Iwai, S., 1977. The hydrogen bonding of artinite. Acta Crystallogr. B Struct. Crystallogr. Cryst. Chem. 33 (12), 3951–3953.

Alexander, G., Maroto-Valer, M.M., Gafarova-Aksoy, P., 2007. Evaluation of reaction variables in the dissolution of serpentine for mineral carbonation. Fuel 86 (1–2), 273–281. https://doi.org/10.1016/j.fuel.2006.04.034.

Andreani, M., Baronnet, A., Boullier, A.M., Gratier, J.P., 2004. A microstructural study of a "crack-seal" type serpentine vein using SEM and TEM techniques. Eur. J. Mineral 16 (4), 585–595. https://doi.org/10.1127/0935-1221/2004/0016-0585.

Andreani, M., Mével, C., Boullier, A.M., Escartin, J., 2007. Dynamic control on serpentine crystallisation in veins: constraints on hydration processes in oceanic peridotites. G-cubed 8 (2). https://doi.org/10.1029/2006GC001373.

Andreani, M., Grauby, O., Baronnet, A., Munoz, M., 2008. Occurrence, composition and growth of polyhedral serpentine. Eur. J. Mineral 20 (2), 159–171. https://doi.org/10.1127/0935-1221/2008/0020-1801.

Baron, F., Sc Pushparaj, S., Fontaine, C., V Sivaiah, M., Decarreau, A., Petit, S., 2016. Microwave-assisted hydrothermal synthesis of Ni-Mg layered silicate clays. Curr. Microwav Chem. 3 (1), 85–89. https://doi.org/10.2174/2213335602666150317233416.

Berner, R.A., Lasaga, A.C., Garrels, R.M., 1983. Carbonate-silicate geochemical cycle and its effect on atmospheric carbon dioxide over the past 100 million years. Am. J. Sci. 283 (7). https://doi.org/10.2475/ajs.283.7.641.

Birle, J.D., Gibbs, G.V., Moore, P.B., Smith, J.V., 1968. Crystal structures of natural olivines. Am. Mineral.: J. Earth Planetary Mater. 53 (5–6), 807–824.

Bloise, A., Belluso, E., Barrese, E., Miriello, D., Apollaro, C., 2009. Synthesis of Fe-doped chrysotile and characterisation of the resulting chrysotile fibers. Cryst. Res. Technol.: J. Exper. Indust. Crystall. 44 (6), 590–596. https://doi.org/10.1002/crat.200900135.

Bloise, A., Belluso, E., Fornero, E., Rinaudo, C., Barrese, E., Capella, S., 2010. Influence of synthesis conditions on growth of Ni-doped chrysotile. Microporous Mesoporous Mater. 132 (1–2), 239–245. https://doi.org/10.1016/j.micromeso.2010.03.003.

Boschi, C., Bedini, F., Baneschi, I., Rielli, A., Baumgartner, L., Perchiazzi, N., et al., 2019. Spontaneous serpentine carbonation controlled by underground dynamic microclimate at the montecastelli copper mine, Italy. Minerals 10 (1), 1.

Brindley, G.W., Wan, H.M., 1975. Compositions, structures, and thermal behavior of nickel-containing minerals in the lizardite-nepouite series. Am. Mineral.: J. Earth Planetary Mater. 60 (9–10), 863–871.

Campione, M., Corti, M., D'Alessio, D., Capitani, G., Lucotti, A., Yivlialin, R., et al., 2024. Microwave-driven carbonation of brucite. J. CO2 Util. 80, 102700. https://doi.org/10.1016/j.jcou.2024.102700.

Campione, M., D'Alessio, D., Corti, M., Capitani, G., Lucotti, A., Tommasini, M., et al., 2025. Catalytic activity of solution additive anions for magnesite and calcite precipitation in microwave-assisted mineral carbonation experiments. Adv. Energy Sustain. Res. 6, 2500046. https://doi.org/10.1002/aesr.202500046.

Cavallo, A., 2018. Serpentinitic waste materials from the dimension stone industry: serpentinitic waste materials from the dimension stone industry: characterization, possible reuses and critical issues. Resour. Policy 59, 17–23. https://doi.org/10.1016/j.resourpol.2018.08.003.

Catti, M., Ferraris, G., Hull, S., Pavese, A., 1995. Static compression and H disorder in brucite, Mg (OH) 2, to 11 GPa: a powder neutron diffraction study. Phys. Chem. Miner. 22 (3), 200–206. https://doi.org/10.1007/BF00202300.

Daval, D., Sissmann, O., Menguy, N., Saldi, G.D., Guyot, F., Martinez, I., et al., 2011. Influence of amorphous silica layer formation on the dissolution rate of olivine at 90 C and elevated pCO2. Chem. Geol. 284 (1–2), 193–209. https://doi.org/10.1016/j.chemgeo.2011.02.021.

Devouard, B., Baronnet, A., Van Tendeloo, G., Amelinckx, S., 1997. First evidence of synthetic polygonal serpentines. European J. Mineralogy-Ohne Beihefte 9 (3), 539–546.

Evans, B.W., 2004. The serpentinite multisystem revisited: chrysotile is metastable. Int. Geol. Rev. 46 (6), 479–506. https://doi.org/10.2747/0020-6814.46.6.479.

Falini, G., Foresti, E., Gazzano, M., Gualtieri, A.F., Leoni, M., Lesci, I.G., Roveri, N., 2004. Tubular-shaped stoichiometric chrysotile nanocrystals. Chem.–Eur. J. 10 (12), 3043–3049. https://doi.org/10.1002/chem.200305685.

Foresti, E., Hochella Jr, M.F., Kornishi, H., Lesci, I.G., Madden, A.S., Roveri, N., Xu, H., 2005. Morphological and chemical/physical characterisation of fe-doped synthetic chrysotile nanotubes. Adv. Funct. Mater. 15 (6), 1009–1016. https://doi.org/10.1002/adfm.200400355.

Gerdemann, S.J., Dahlin, D.C., O'Connor, W.K., 2003. Carbon dioxide sequestration by aqueous mineral carbonation of magnesium silicate minerals. In: Greenhouse Gas Control Technologies-6th International Conference. Pergamon, pp. 677–682. https://doi.org/10.1016/B978-008044276-1/50108-2.

Grauby, O., Baronnet, A., Devouard, B., Schoumacker, K., Demirdjian, L., 1998. The chrysotile-polygonal serpentine-lizardite suite synthesised from a 3MgO-2SiO2-excess H2O gel. In: The 7th International Symposium on Experimental Mineralogy, Petrology, and Geochemistry, Orléans, Abstracts, vol. 1. Terra Nova, p. 24. *supplement*.

Hamilton, J.L., Wilson, S., Morgan, B., Turvey, C.C., Paterson, D.J., Jowitt, S.M., et al., 2018. Fate of transition metals during passive carbonation of ultramafic mine tailings via air capture with potential for metal resource recovery. Int. J. Greenh. Gas Control 71, 155–167. https://doi.org/10.1016/j.ijggc.2018.02.008.

Hänchen, M., Krevor, S., Mazzotti, M., Lackner, K.S., 2007. Validation of a population balance model for olivine dissolution. Chem. Eng. Sci. 62 (22), 6412–6422. https://doi.org/10.1016/j.ces.2007.07.065.

Hazen, R.M., 1976. Effects of temperature and pressure on the cell dimension and X-ray temperature factors of periclase. Am. Mineral. 61 (3–4), 266–271.

Herzog, H., 2002. Carbon Sequestration via Mineral Carbonation: Overview and Assessment 14 March 2002.

Hugh-Jones, D.A., Angel, R.J., 1994. A compressional study of MgSiO3 orthoenstatite up to 8.5 GPa. Am. Mineral. 79 (5–6), 405–410.

Ide, T.S., Jessen, K., Orr, F.M., 2007. Storage of CO2 in saline aquifers: effects of gravity, viscous, and capillary forces on amount and timing of trapping. Int. J. Greenh. Gas Control 1, 481–491. https://doi.org/10.1016/S1750-5836(07)00091-6.

IPCC, 2023. AR6 synthesis report: climate change 2023 — IPCC, AR6 synth. Rep. Clim. Chang. 2023 — IPCC https://www.ipcc.ch/report/ar6/syr/.
Jancar, B., Suvorov, D., 2005. The influence of hydrothermal-reaction parameters on the formation of chrysotile nanotubes. Nanotechnology 17 (1), 25. https://doi.org/10.1088/0957-4484/17/1/005.
Jonckbloedt, R.C.L., 1998. Olivine dissolution in sulphuric acid at elevated temperatures—implications for the olivine process, an alternative waste acid neutralizing process. J. Geochem. Explor. 62 (1–3), 337–346. https://doi.org/10.1016/S0375-6742(98)00002-8.
Kelemen, P.B., Matter, J., 2008. In situ carbonation of peridotite for CO2 storage. Proc. Natl. Acad. Sci. 105 (45), 17295–17300. https://doi.org/10.1073/pnas.0805794105.
Korytkova, E.N., Maslov, A.V., Pivovarova, L.N., Polegotchenkova, Y.V., Povinich, V.F., Gusarov, V.V., 2005a. Synthesis of nanotubular $Mg_3Si_2O_5(OH)_4$ - $Ni_3Si_2O_5(OH)_4$ silicates at elevated temperatures and pressures. Inorg. Mater. 41, 743–749. https://doi.org/10.1007/s10789-005-0202-1.
Korytkova, E.N., Pivovarova, L.N., Drozdova, I.A., Gusarov, V.V., 2005b. Synthesis of nanotubular nickel hydrosilicates and nickel-magnesium hydrosilicates under hydrothermal conditions. Glass Phys. Chem. 31, 797–802. https://doi.org/10.1007/s10720-005-0127-4.
Korytkova, E.N., Pivovarova, L.N., 2010. Hydrothermal synthesis of nanotubes based on $(Mg, Fe, Co, Ni)_3Si_2O_5(OH)_4$ hydrosilicates. Glass Phys. Chem. 36, 53–60. https://doi.org/10.1134/S1087659610010104.
Kwak, J.H., Hu, J.Z., Turcu, R.V.F., Rosso, K.M., Ilton, E.S., Wang, C., Sears, J.A., Engelhard, M.H., Felmy, A.R., Hoyt, D.W., 2011. The role of H2O in the carbonation of forsterite in supercritical CO2. Int. J. Greenh. Gas Control 5, 1081–1092. https://doi.org/10.1016/j.ijggc.2011.05.013.
Lacinska, A.M., Styles, M.T., Bateman, K., Hall, M., Brown, P.D., 2017. An experimental study of the carbonation of serpentinite and partially serpentinised peridotites. Front. Earth Sci. 5, 37. https://doi.org/10.3389/feart.2017.00037.
Lackner, K.S., Wendt, C.H., Butt, D.P., Joyce Jr, E.L., Sharp, D.H., 1995. Carbon dioxide disposal in carbonate minerals. Energy 20 (11), 1153–1170. https://doi.org/10.1016/0360-5442(95)00071-N.
Lafay, R., Montes-Hernandez, G., Janots, E., Chiriac, R., Findling, N., Toche, F., 2013. Nucleation and growth of chrysotile nanotubes in H2SiO3/MgCl2/NaOH medium at 90 to 300 C. Chem.–Eur. J. 19 (17), 5417–5424. https://doi.org/10.1002/chem.201204105.
Lafay, R., Fernandez-Martinez, A., Montes-Hernandez, G., Auzende, A.L., Poulain, A., 2016. Dissolution-reprecipitation and self-assembly of serpentine nanoparticles preceding chrysotile formation: insights into the structure of proto-serpentine. Am. Mineral. 101 (12), 2666–2676. https://doi.org/10.2138/am-2016-5772.
Lesci, I.G., Balducci, G., Pierini, F., Soavi, F., Roveri, N., 2014. Surface features and thermal stability of mesoporous Fe doped geoinspired synthetic chrysotile nanotubes. Microporous Mesoporous Mater. 197, 8–16. https://doi.org/10.1016/j.micromeso.2014.06.002.
Liu, Y., Liu, P., Hu, C., 2018. Hydrothermally assisted synthesis of pure-phase and well-dispersed forsterite nanopowders. Ceram. Int. 44 (18), 23339–23343. https://doi.org/10.1016/j.ceramint.2018.09.120.
Lu, X., Carroll, K.J., Turvey, C.C., Dipple, G.M., 2022. Rate and capacity of cation release from ultramafic mine tailings for carbon capture and storage. Appl. Geochem. 140, 105285. https://doi.org/10.1016/j.apgeochem.2022.105285.
Matter, J.M., Kelemen, P.B., 2009. Permanent storage of carbon dioxide in geological reservoirs by mineral carbonation. Nat. Geosci. 2 (12), 837–841. https://doi.org/10.1038/ngeo683.
McDonald, A., Scott, B., Villemure, G., 2009. Hydrothermal preparation of nanotubular particles of a 1: 1 nickel phyllosilicate. Microporous Mesoporous Mater. 120 (3), 263–266. https://doi.org/10.1016/j.micromeso.2008.11.013.
McKelvy, M.J., Chizmeshya, A.V.G., Diefenbacher, J., Béarat, H., Wolf, G., 2004. Exploration of the role of heat activation in enhancing serpentine carbon sequestration reactions. Environ. Sci. Technol. 38, 6897–6903. https://doi.org/10.1021/es049473m.
Mellini, M., 1982. The crystal structure of lizardite 1 T: hydrogen bonds and polytypism. Am. Mineral. 67 (5–6), 587–598.
Monguzzi, A., Lesci, I.G., Capitani, G.C., Santo, N., Roveri, N., Campione, M., 2014. Mineral–organic hybrid nanotubes as highly sensitive solid state optical chemical sensors. Phys. Chem. Chem. Phys. 16 (6), 2491–2498. https://doi.org/10.1039/C3CP54467B.
Normand, C., Williams-Jones, A.E., Martin, R.F., Vali, H., 2002. Hydrothermal alteration of olivine in a flow-through autoclave: nucleation and growth of serpentine phases. Am. Mineral. 87 (11–12), 1699–1709. https://doi.org/10.2138/am-2002-11-1220.
Norouzpour, M., Santos, R.M., Chiang, Y.W., 2025. Activation methods for enhancing CO2 mineralization via mine tailings—A critical review. Carbon Capture Sci. Technol. 15, 100430. https://doi.org/10.1016/j.ccst.2025.100430.
O'Connor, W.K., Dahlin, D.C., Nilsen, D.N., Rush, G.E., Gerdemann, S.J., Walters, R.P., Turner, P.C., 2001. Carbon dioxide sequestration: aqueous mineral carbonation studies using olivine and serpentine. In: National Energy Technology Laboratory: Mineral Carbonation Workshop. Pittsburgh, PA, August 8.
O'Connor, W.K., Dahlin, D.C., Rush, G.E., Dahlin, C.L., Collins, W.K., 2002. Carbon dioxide sequestration by direct mineral carbonation: process mineralogy of feed and products. Mining, Metall. Explorat. 19, 95–101. https://doi.org/10.1007/BF03403262.
O'Connor, W.K., Dahlin, D.C., Rush, G.E., Gerdemann, S.J., Penner, L.R., 2004. *Energy and economic considerations for ex-situ and aqueous mineral carbonation* (No. DOE/ARC-2004-028). Albany Research Center (ARC). Albany, OR (United States).
Park, A.H.A., Jadhav, R., Fan, L.S., 2003. CO2 mineral sequestration: chemically enhanced aqueous carbonation of serpentine. Can. J. Chem. Eng. 81 (3-4), 885–890. https://doi.org/10.1002/cjce.5450810373.
Pokrovsky, O.S., Schott, J., 2000. Kinetics and mechanism of forsterite dissolution at 25 C and pH from 1 to 12. Geochem. Cosmochim. Acta 64 (19), 3313–3325. https://doi.org/10.1016/S0016-7037(00)00434-8.
Raade, G., 1970. Dypingite, a new hydrous basic carbonate of magnesium, from Norway. Am. Mineral.: J. Earth Planetary Mater. 55 (9–10), 1457–1465.
Rashid, M.I., Benhelal, E., Farhang, F., Oliver, T.K., Rayson, M.S., Brent, G.F., Stockenhuber, M., Kennedy, E.M., 2019. Development of concurrent grinding for application in aqueous mineral carbonation. J. Clean. Prod. 212, 151–161. https://doi.org/10.1016/j.jclepro.2018.11.189.
Sanna, A., Uibu, A.M., Caramanna, B.G., Kuusikb, R., Maroto-Valerac, M.M., 2014. A review of mineral carbonation technologies to sequester CO2. Chem. Soc. Rev. 43, 8049–8080. https://doi.org/10.1039/C4CS00035H.
Soler, J.M., Cama, J., Galí, S., Meléndez, W., Ramírez, A., Estanga, J., 2008. Composition and dissolution kinetics of garnierite from the Loma de Hierro Ni-laterite deposit, Venezuela. Chem. Geol. 249, 191–202. https://doi.org/10.1016/j.chemgeo.2007.12.012.
Sissmann, O., Daval, D., Brunet, F., Guyot, F., Verlaguet, A., Pinquier, Y., Findling, N., Martinez, I., 2013. The deleterious effect of secondary phases on olivine carbonation yield: insight from time-resolved aqueous-fluid sampling and FIB-TEM characterization. Chem. Geol. 357, 186–202. https://doi.org/10.1016/j.chemgeo.2013.08.031.
Shikazono, N., Okuyama, Y., Umemura, T., Kashiwagi, H., 2014. Dissolution experiments of serpentinite and kinetic modeling of CO2 behavior for underground sequestration of CO_2 in deep serpentinite aquifers. J. MMIJ 130 (7), 396–403.
Viti, C., Mellini, M., 1998. Mesh textures and bastites in the Elba retrograde serpentinites. Eur. J. Mineral 10 (6), 1341–1359.
Walker, D., Verma, P.K., Cranswick, L.M., Jones, R.L., Clark, S.M., Buhre, S., 2004. Halite-sylvite thermoelasticity. Am. Mineral. 89 (1), 204–210. https://doi.org/10.2138/am-2004-0124.
Wang, F., Dreisinger, D., 2022. Carbon mineralization with concurrent critical metal recovery from olivine. Proc. Natl. Acad. Sci. 119 (32), e2203937119. https://doi.org/10.1073/pnas.2203937119.
White, W.B., Silsbee, M.R., Kearns, B.J., 2004. Reaction Mechanisms of Magnesium Silicates with Carbon Dioxide in Microwave Fields. Pennsylvania State University (US). https://doi.org/10.2172/826203, 2004.
Wicks, F.J., Whittaker, E.J.W., 1975. A reappraisal of the structures of the serpentine minerals. Can. Mineral. 13 (3), 227–243.
Yada, K., 1971. Study of microstructure of chrysotile asbestos by high-resolution electron microscopy. Acta Crystallogr. Sect. A Cryst. Phys. Diffr. Theor. Gen. Crystallogr. 27 (6), 659–664.
Yada, K., Iishi, K., 1974. Serpentine minerals hydrothermally synthesised and their microstructures. J. Cryst. Growth 24, 627–630.
Yada, K., Iishi, K., 1977. Growth and microstructure of synthetic chrysotile. Am. Mineral. 62 (9–10), 958–965.
Yamamoto, G.I., Kyono, A., Okada, S., 2022. Thermal decomposition process of dypingite $Mg_5(CO_3)_4(OH)_2 \cdot 5H_2O$. Mater. Lett. 308, 131125. https://doi.org/10.1016/j.matlet.2021.131125.